

A length scale insensitive phase field model for brittle fracture of hyperelastic solids

Tushar Kanti Mandal^{a,*}, Abhinav Gupta^b, Vinh Phu Nguyen^{a,*}, Rajib Chowdhury^b, Alban de Vaucorbeil^c

^a Department of Civil Engineering, Monash University, Clayton, Victoria 3800, Australia

^b Department of Civil Engineering, IIT Roorkee, India

^c Institute of Frontier Materials, Deakin University, Geelong, VIC 3216, Australia

ARTICLE INFO

Keywords:

Phase-field theory
Variational approach to fracture
Rubber
Hyperelasticity
Brittle fracture
PF-CZM.

ABSTRACT

Fracture of hyperelastic materials such as synthetic rubber, hydrogels, textile fabrics is an essential problem in many engineering fields. The computational simulation of such a fracture is complicated, but the use of phase field models (PFMs) is promising. Indeed, in PFMs, sharp cracks are not treated as discontinuities; instead, they are approximated as thin damage bands. Thus, PFMs can seamlessly model complex crack patterns like branching, merging, and fragmentation. However, previous PFMs for hyperelastic materials, which are mostly based on a PFM with a simple quadratic degradation function without any user-defined parameters, provide solutions that are sensitive to a length scale (that controls the width of the damage band). The current practice of considering this length scale as a material parameter suffers from two issues. First, such a calculated length scale might be too big (compared with the problem dimension) to provide meaningful crack patterns. Second, it might be too small, which results in undesirable computationally expensive simulations. This paper presents a length scale insensitive PFM for brittle fracture of hyperelastic materials. This model is an extension of the model of Wu (2017) with a material parameter dependent rational degradation function, which converges to Cohesive Zone Model (CZM) at least for 1D problems (Wu and Nguyen, 2018), and also can deal with crack nucleation and propagation simultaneously. Results of mode-I and mixed-mode fracture problems obtained with the method of finite elements are in good agreement with previous findings and independent of the discretization resolution. Most importantly, they are independent of the incorporated length scale parameter. Moreover, preliminary results show that the proposed model is as efficient as, if not more than the previous models.

1. Introduction

Predicting the initiation and propagation of cracks is a major engineering concern for the safety of existing structures and the better design of fracture-resilient materials. This paper focuses on hyperelastic materials – those materials that respond elastically when subjected to very large strains – which are abundant in engineering applications and nature. Hyperelastic materials such as synthetic rubbers, hydrogels, textile fabrics have been used for their superior performance (e.g. strength, long-lasting, water-resistance, and heat resistance) for various applications. Typical examples are tires, seals and gaskets in automobiles and aircraft; door-

* Corresponding authors.

E-mail addresses: tushar.mandal@monash.edu (T.K. Mandal), phu.nguyen@monash.edu (V.P. Nguyen).

seals in spaceships [27]; active sonar, torpedo ejection system in submarines [20]. Moreover, a rubber-like elastomer is abundant in nature in the form of biological tissues – important objects of research in biomechanics and biomedical engineering [40,39,29,78,26]. Besides engineering interests, the hyperelastic fracture has attracted researches from various scientific backgrounds to understand the complex interplay between nonlinear elasticity and stress singularities *i.e.*, stress at the crack tip where the radius is nearly zero, would tend to infinity [19,18,55].

Computational modeling of fracture processes – processes in which a material is separated, by the appearance of some sharp cracks, into two or more pieces under the action of stress – constitutes an indispensable tool to predict the failure of cracked structures, for which full-scale experiments are either too costly or even impracticable and analytical solutions seldom exist. Furthermore, modeling helps to understand the fracture processes, which in turn might lead to the development of improved fracture-resilient materials. Recently, the phase field fracture model (PFM) is receiving lots of attention. This model, set forth by [15], is an implementation of the *variational approach to brittle fracture* [24] – a generalization of linear elastic fracture mechanics pioneered by Griffith [28], Irwin [41].

In a PFM, the sharp crack is regularized (or replaced) by a diffuse damage band of finite thickness via the introduction of a continuous scalar field (referred to as phase field or damage field). This field discriminates the intact and broken material. The width of the damage band is governed by a small positive length scale parameter b and when $b \rightarrow 0$, the solution of PFM converges to the fracture mechanics solution according to the Γ -convergence theorem [17]. Wu et al. [89] have numerically demonstrated this convergence by comparing the phase field solutions with solutions of a discrete fracture model. Linear elastic fracture mechanics is a discrete fracture model whereas a PFM is a continuum fracture model. But bear in mind that both of them are within the framework of continuum mechanics [56].

Phase-field models enable the simulation of three dimensional complex fracture problems *e.g.* those involving crack branching and crack merging using a fixed finite element (FE) mesh with a straightforward implementation: one just needs to solve two partial differential equations, one for the displacement field and the other for the phase field, both with the well established standard continuum finite elements. This is in contrast to discrete fracture models based on linear elastic fracture mechanics in which one has to track the evolving crack surfaces, a difficult task and to adopt specialized finite elements [77].

The good performance of PFMs have been demonstrated by various applications: brittle fracture [65,66,86], quasi-brittle fracture [62,85,23,37,57,58], ductile fracture [5,14], dynamic brittle fracture [16,13,79,69,59], and multi-physics fracture [67,49,61,90], to quote only a few. We refer to Wu et al. [88] for a review of PFMs.

To set the context for the paper, we review common PFMs for small strain brittle and quasi-brittle fracture in Section 1.1. They are the starting point for PFMs for hyperelastic fracture reviewed in Section 1.2. Then, our contributions are stated in Section 1.3.

1.1. Common small strain phase field fracture models

According to PFMs for quasi-static fracture of solids under the infinitesimal strain regime, the displacement field \mathbf{u} and damage field d are minimizers of the following total energy functional of the solid

$$\mathcal{E}(\mathbf{u}, d) = \int_{\Omega_0} [\omega(d)\psi_0^+(\epsilon(\mathbf{u})) + \psi_0^-(\epsilon(\mathbf{u}))] dV + \int_{\Omega_0} \frac{G_f}{c_\alpha} \left[\frac{1}{b} \alpha(d) + b(\nabla d \cdot \nabla d) \right] dV - \mathcal{P}(\mathbf{u}) \quad (1.1)$$

where the first integral is the stored strain energy, the second one denotes the fracture energy à la Griffith, and $\mathcal{P}(\mathbf{u})$ denotes the external work, G_f is the fracture toughness; $\omega(d)$ is the stress/energetic degradation function and $\alpha(d)$ represents the crack geometric function. The positive and negative parts of the strain energy density are denoted by $\psi_0^+(\epsilon(\mathbf{u}))$ and $\psi_0^-(\epsilon(\mathbf{u}))$, respectively. These positive/negative parts play an important role in capturing the tension/compression asymmetry of fracture – fracture does not occur in domains under compression.

The three most common (second order) PFMs are listed in Table 1. The AT2 model, developed by Bourdin et al. [15], Miehe et al. [65] is probably the most widely used PFM in engineering even though it lacks an elastic domain *i.e.*, damage becomes non-zero immediately when the load (no matter how small it is) is applied. The AT1 model of Pham et al. [74], possessing an elastic domain, is getting more attention. While both the AT1 and AT2 models apply only to brittle fracture, the PF-CZM (phase field regularized cohesive zone model) of Wu [85], Wu and Nguyen [86] is the first PFM that applies to both brittle and cohesive fracture. Contrary to

Table 1

Common phase field models for small strain brittle and cohesive fracture. The AT2 has an infinite support of the damage field whereas the AT1 and PF-CZM have a finite support. TSL is short for traction-separation law, see *e.g.* [21,72]. Irwin's internal length is defined as $l_{ch} := E_0 G_f / f_t^2$, with E_0 being Young's modulus of the material; f_t and G_f being the failure strength and fracture energy (toughness), respectively. Notice that the models were presented in chronological order. The PF-CZM, albeit with its complex degradation function, is more efficient than the AT1/2 [58].

model	$\alpha(d)$	$\omega(d)$	fracture type	length-scale	sup.	Parameters	Efficiency
AT2	d^2	$(1-d)^2$	brittle	$b = \frac{27}{256} l_{ch}$	∞	E_0, ν_0, G_f, b	😊
AT1	d	$(1-d)^2$	brittle	$b = \frac{3}{8} l_{ch}$	$4b$	E_0, ν_0, G_f, b	😊
PF-CZM	$2d - d^2$	$\frac{(1-d)^p}{(1-d)^p + Q(d)}$	brittle/cohesive	numerical num.	πb	$E_0, \dots + \text{TSL}$	😊😊

Table 2

Variationally (in) consistent isotropic model and anisotropic models: E_0 is the fourth-order elasticity tensor, $\bar{\sigma}_1$ denotes the first major principle value of the effective stress tensor $\bar{\sigma} := E_0 : \epsilon$; Macaulay brackets $\langle \cdot \rangle$ are defined as $\langle x \rangle = \max(x, 0)$.

	VC isotropic	VIC isotropic (hybrid)	VC anisotropic
σ	$\omega(d)E_0 : \epsilon$	$\omega(d)E_0 : \epsilon$	$\omega(d)\frac{\partial\psi_0^+}{\partial\epsilon} + \frac{\partial\psi_0^-}{\partial\epsilon}$
\bar{Y}	$\frac{1}{2}\epsilon : E_0 : \epsilon$	$\frac{1}{2E_0}\left\langle\bar{\sigma}_1\right\rangle^2$	$\psi_0^+(\epsilon)$

the AT1/2 models, it is numerically less sensitive, if not insensitive, to the length scale parameter for static fracture [57,58], dynamic fracture [69,59] and multi-field fracture [90]. Moreover, it is also not mesh biased due to its rational degradation function [58].

Remark 1.1. Any model with material fracture energy G_f owes an internal length scale, i.e., Irwin's length $l_{ch} = E_0 G_f / f_i^2$. However, in AT1/2, the regularization length scale b has to be dependent upon Irwin's length scale otherwise the tensile strength f_i cannot be matched. In other words, the interentanglement between b and l_{ch} results in the lack of a second length scale which is mandatory for a smeared or regularized approach (only the discontinuous approach such as LEFM and CZM works with the single Irwin's length scale). \square

For each model in Table 1, there are different formulations regarding the stress σ and the effective crack driving force \bar{Y} , to model the tension/compression asymmetry of fracture. These formulations can be categorized as variationally consistent and variationally inconsistent models (Table 2). Variationally consistent (VC) isotropic models cannot capture this asymmetry and thus limited to mode-I fracture problems. Variationally inconsistent (VIC) isotropic models, which Ambati et al. [4] named hybrid models, and anisotropic models [7,65,91] can prevent fracture in compression domains. There exist some ψ_0^+/ψ_0^- splits and the most common splits are the volumetric-deviatoric split of Amor et al. [7] and the spectral decomposition of Miehe et al. [65]. Recently, Wu et al. [91] developed a split based on a positive/negative projection in energy norm. Compared to other similar schemes, the resulting tensile part of the free energy density is minimized and thus this split is consistent with the spirit of the variational approach to fracture.

1.2. Related works on finite deformation phase field fracture models

Application of phase field method to hyperelastic fracture is comparatively scarce compared to a large body of work on elastic fracture. Piero et al. [76] were the first to report a hyperelastic PFM: it is an extension of the AT2 model. In the extension, the fracture energy in Eq. (1.1) was kept unchanged and only a strain energy appropriate for hyperelastic solids replaced the elastic stored strain energy. No strain energy density split was used as the authors focused on tensile only mode-I fracture problems. This hyperelastic PFM was followed by subsequent works.

Miehe and Schäanzel [64] has coupled the AT2 model with Neo-Hookean hyperelasticity to model mode-I fracture of rubbery polymers using a variationally consistent isotropic formulation. In the same year, Hesch and Weinberg [33] has proposed a multiplicative split of stretch to capture the tension/compression asymmetry. This approach, however, suffers from numerical convergence issues [14] due to non-polyconvexity of the strain energy functional. To overcome this problem, Hesch et al. [34] has proposed an additive split of the strain energy based on the principal invariants of strain measures maintaining the polyconvexity of the strain energy functional. Although mathematically attractive, Hesch et al.'s method lacks physical interpretation. Yet another additive split of the strain energy, but now based on principal stretches was presented in Tang et al. [82] and Zhang et al. [94]. More recently, Loew et al. [51] have developed a rate-dependent AT2 model for fracture of rubbers. This is an extension of Miehe and Schäanzel's model [64] in which rate-dependency was incorporated in the bulk response and in the damage evolution.

Hyperelastic phase field models have been applied for different fracture problems. A finite deformation ductile fracture AT2 model has been demonstrated in Borden et al. [14], Ambati et al. [5] using the volumetric-deviatoric split of Amor et al. [7]. Fracture and healing of elastomers has been studied in Kumar et al. [48] and Talamini et al. [81] presented a micro-mechanically motivated crack driving force for fracture of rubbery polymers using a hyperelastic AT2 model. PFMs with anisotropic surface energy have been reported in Clayton and Knap [19], Gültekin et al. [29], Raina and Miehe [78], Gültekin et al. [30] with applications for fracture of biological tissues. Complex anisotropic fracture of orientation-dependent natural materials have been simulated in Yin et al. [93].

1.3. Contributions of this paper

All previous hyperelastic PFMs were based on the AT2 model and thus inherit its limitations: (i) incorrect damage initiation for problems without singularities e.g. corners, blunt notches, etc. [83], (ii) length scale sensitive results [58] and (iii) large damage band widths. Regarding the second issue, one can consider the length scale as a material parameter [74,68]. But, Mandal et al. [58] showed that such length scales can be too small (resulting in large discrete problems which are expensive to solve) or too large compared with the problem dimension to provide meaningful crack patterns. The third limitation only arises for problems where a crack tip goes into a nearby hole (where it should not).

Therefore, the aim of the paper is to present a PFM that overcomes all the issues of AT2 models. The idea is to extend the small

strain PF-CZM to hyperelastic solids. The methodology is conceptually simple: the fracture energy term in Eq. (1.1) is kept unmodified with the crack geometric function and the stress degradation function of the PF-CZM (Table 1), and the stored strain energy taken from Miehe and Schänzel [64], Tang et al. [82].

We present the following concrete contributions:

- a unified phase field fracture framework for hyperelastic solids that covers the available AT2, and the AT1 and the PF-CZM which are new – this can be considered as the hyperelastic extension of unified PFM of Wu [85];
- analytical solutions for homogeneous damage and stress fields of a softening hyperelastic bar;
- formulas relating the length scale to the material tensile strength for the AT1/2 similar to the ones given in Table 1;
- a hybrid formulation using the positive part of the strain energy;
- an implicit-explicit solver – an implicit static solver is used prior to damage localization and an explicit dynamics solver is used thereafter to resolve the non-convergence issue of the implicit alternating minimization solver of Bourdin et al. [15];
- computer implementation of the proposed formulation using both the traditional way (*i.e.*, we manually coded the FE vectors and matrices ourselves) and FEniCS [1,32]. The latter automatically generates the codes for the FE vectors and matrices.

Our primary goal of this work is the tensile fracture of hyperelastic solids and modeling compression failure is beyond the scope of current research. For the sake of simplicity, we adopt compressible hyperelastic models. Usefulness and complexities related to incompressible models for phase field fracture are beyond the scope of the paper. We refer to Mang et al. [60], Ye et al. [92] for recent work on this topic including Hu-Washizu mixed formulation. Moreover, only fracture of solids with isotropic surface energy (*i.e.*, orientation-independent fracture energy) is considered. Finally, our model is rate-independent.

Remark 1.2. Recently, Loew et al. [52] also have presented a hyperelastic PF-CZM for fatigue fracture of rubber – which is significantly different from the current study. Firstly, the primary goal of their work was to fit PF-CZM parameter(s) to the extensive experimental results available and apply for fatigue fracture; whereas we have provided the mathematical framework to estimate the PF-CZM parameters from minimal material parameters *e.g.* Young's modulus of elasticity E_0 , tensile strength f_t , and fracture energy G_f ; and also explained why PF-CZM provides a length scale insensitive global load-deformation response through an analytical calculation. Secondly, they have considered mode-I fracture with total strain energy; whereas we have considered the positive-negative split of strain energy to simulate mixed-mode fracture correctly. Third, the considered neo-hookean material models in the current work are also different. \square

1.4. Outline and notation

The remainder of this paper is structured as follows. Section 2 provides the mathematical formulation in a total Lagrangian framework of the proposed model. Section 3 presents the adopted Neo-Hookean materials. Section 4 presents the analytical homogeneous solutions for a bar in uniaxial tension. Next, Section 5 describes the numerical implementation using finite elements. Representative numerical examples are given in Section 6 for multiple brittle and quasi-brittle fracture benchmark problems. The most relevant conclusions are drawn in Section 7. Reproducibility of results and implementation differences between two FE packages feFRAC and FEniCS are provided in Appendix A. Appendix B outlines the implementation of plane-stress state in hyperelasticity. Derivation of strain energy split is provided in Appendix C. Appendix D provides some finite element implementation details.

Notation. Compact tensor notation is used in the theoretical part of this paper. As general rules, scalars are denoted by italic light-face Greek or Latin letters (*e.g.* a or λ); vectors, second- and fourth-order tensors are signified by italic boldface minuscule, majuscule and blackboard-bold majuscule characters like α , A and \mathbb{A} , respectively. The inner products with single and double contractions are denoted by “ \cdot ” and “ $\cdot\cdot$ ”, respectively. Symbols with a bar on top ($\bar{\square}$) denote effective quantities whereas ones with an asterisk (\square^*) represent prescribed quantities. In the numeric part of finite elements, Voigt notation is adopted where vectors and second-order tensors are denoted by boldface minuscule and majuscule letters like \mathbf{a} and \mathbf{A} , respectively. The symbol \square^T denotes the transpose operator, $f'(x)$ represents the first derivative of $f(x)$ with respect to x and \dot{f} represents the first derivative of f with respect to time.

2. Variational formulation of a hyperelastic phase field fracture model

We present herein the governing equations of a generic phase field model for brittle fracture of hyperelastic solids. By generic, we meant the model covers all PFMs introduced in Table 1 and applies to any hyperelastic solids. Even though we consider only static fracture later in the numerical examples section (Section 6), inertial effects are included not only for generality but also for the explicit dynamics solver being used. Similar to previous work, we also adopt a total Lagrangian formulation. And the derivation is based on the Hamilton's principle of least action.

We consider a cracking solid of which the (original undeformed) reference configuration is denoted by $\Omega_0 \subset \mathbb{R}^{n_{\text{dim}}}$ ($n_{\text{dim}} = 1, 2, 3$). The solid contains some sharp cracks and/or interfaces $S \subset \mathbb{R}^{n_{\text{dim}}-1}$, see Fig. 1a. The solid particles are labeled by their material coordinates X and the solid is kinematically described by the displacement field $\mathbf{u}(X, t): \Omega_0 \times [0, T] \rightarrow \mathbb{R}^{n_{\text{dim}}}$ in time $t \in [0, T] \in \mathbb{R}_+$ for some time interval $T > 0$. The external boundary is split into two disjoint (or non-overlapping) parts $\partial\Omega_{0,u}$ and $\partial\Omega_{0,r}$.

To describe the finite deformation kinematics, the Lagrange strain field $\mathbf{E}(X, t)$ and the right Cauchy-Green deformation tensor \mathbf{C} are used. They are defined as: $\mathbf{E}(X, t) := \frac{1}{2}(\mathbf{C} - \mathbf{I})$, $\mathbf{C} := \mathbf{F}^T \mathbf{F}$ where the deformation gradient \mathbf{F} is $\mathbf{F} := \mathbf{I} + \nabla_0 \mathbf{u}(X, t)$ [10]; \mathbf{I} is the

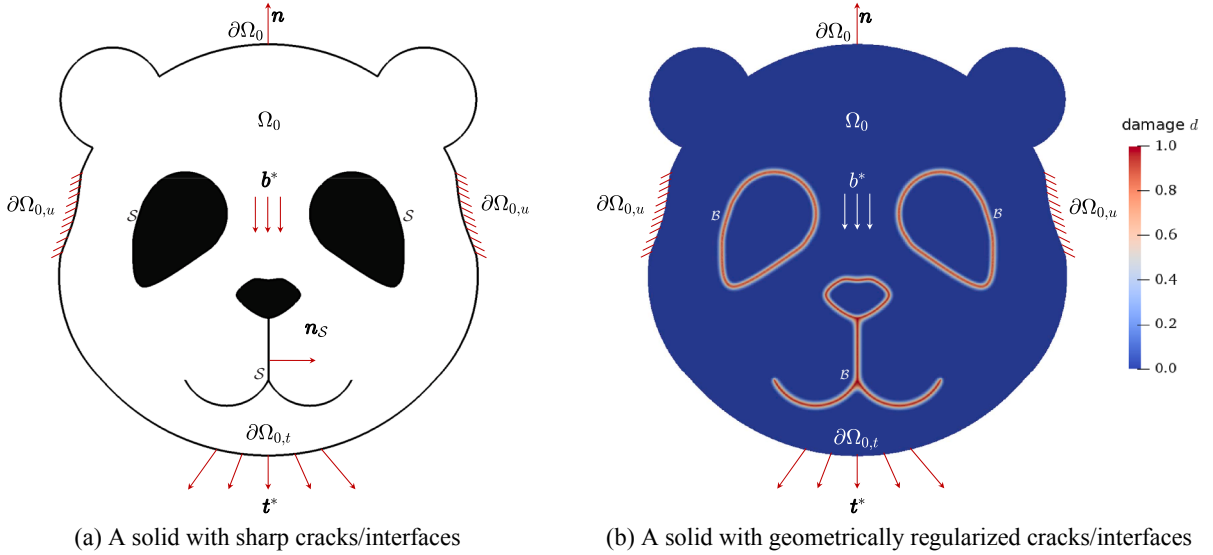


Fig. 1. A cracking solid with sharp cracks/interfaces and the geometric regularization. The external boundary is denoted by $\partial\Omega_0 \subset \mathbb{R}^{n_{\text{dim}-1}}$, with the outward unit normal denoted by vector \mathbf{n} . The distributed body force is denoted by \mathbf{b}^* .

identity second-order tensor and ∇_0 denotes the gradient operator with respect to X .

The main idea of PFM is to approximate the sharp crack S by a diffuse damage band \mathcal{B} (Fig. 1b) where the damage field $d(X, t)$ localises i.e., $0 < d(X, t) \leq 1$ for $X \in \mathcal{B}$. Outside of this damage band, the damage is identically zero. This approximation is referred to as geometric regularization by Miehe et al. [66]. Similar to continuum damage mechanics, see e.g. Kachanov [42], $d = 0$ signifies intact material and $d = 1.0$ labels completely broken material.

With the introduction of a crack surface density function $\gamma(d; \nabla_0 d)$, one can write the Griffith surface energy Ψ_c (a surface integral) as a volume integral [17]

$$\Psi_c := \int_S G_f dA_s \approx \int_{\Omega_0} G_f \gamma(d, \nabla_0 d) dV \quad (2.1)$$

The significance of this equation is that in the second integral the integration domain is unknown whereas in the second equation, the integration domain is known: it is the original domain Ω_0 . Therefore, instead of tracking S as in discrete fracture models – a difficult task [77], one just needs to solve another equation for d on a fixed domain.

Considering a second order¹ rate independent phase field formulation, the crack surface density function $\gamma(d; \nabla_0 d)$ can be expressed as [85]

$$\gamma(d; \nabla_0 d) = \frac{1}{c_\alpha} \left[\frac{1}{b} \alpha(d) + b \nabla_0 d \cdot \nabla_0 d \right] \quad (2.2)$$

where b denotes the length scale for regularization, the scaling parameter c_α and geometric crack function $\alpha(d)$ are given in Section 3.2.

The Lagrangian for the system $\mathcal{L} := \mathcal{K} - (\Psi_s + \Psi_c - \mathcal{P})$ with kinetic energy \mathcal{K} , free energy Ψ_s and external work \mathcal{P} are expressed in the reference configuration as

$$\mathcal{L}(\mathbf{u}, d) = \underbrace{\frac{1}{2} \int_{\Omega_0} \rho \dot{\mathbf{u}} \cdot \dot{\mathbf{u}} dV}_{\mathcal{K}} - \underbrace{\int_{\Omega_0} \psi_s(\mathbf{C}(\mathbf{u}), d) dV}_{\Psi_s} - \underbrace{\int_{\Omega_0} G_f \gamma(d; \nabla_0 d) dV}_{\Psi_c} + \underbrace{\int_{\Omega_0} \mathbf{b}^* \cdot \mathbf{u} dV + \int_{\partial\Omega_0, t} \mathbf{t}^* \cdot \mathbf{u} dA}_{\mathcal{P}} \quad (2.3)$$

Using Hamilton's principle on stationary of the action integral $\mathcal{A} := \int_{t_1}^{t_2} \mathcal{L}(\mathbf{u}, d) dt$ along with the necessary requirement of non-decreasing² and boundedness on the damage field, we obtain the following set of equations for displacement and damage sub-problems,

¹ Second-order PFM involve second derivative of the damage variable d . Higher-order PFM have been presented in e.g. [12] but not considered in this work as second-order models are sufficient for modeling solids with isotropic fracture energies.

² based on Griffith's theory of fracture: crack is non-decreasing and first-order action variation is non-negative [50].

$$\int_{\Omega_0} S(\mathbf{u}, d) \mathbf{F}^T(\mathbf{u}) : \nabla_0 \delta \mathbf{u} dV + \int_{\Omega_0} \rho \ddot{\mathbf{u}} \cdot \delta \mathbf{u} dV = \int_{\partial\Omega_{0,t}} \mathbf{t}^* \cdot \delta \mathbf{u} dA + \int_{\Omega_0} \mathbf{b}^* \cdot \delta \mathbf{u} dV \quad (2.4a)$$

$$\int_{\Omega_0} \left[\omega'(d) \bar{Y} \delta d + \frac{G_f}{c_\alpha} \left(\frac{\alpha'(d)}{b} \delta d + 2b \nabla_0 d \cdot \nabla_0 \delta d \right) \right] dV \geq 0 \quad (2.4b)$$

with the second Piola-Kirchoff stress $\mathbf{S} := 2 \frac{\partial \psi}{\partial \mathbf{F}}$ and the effective crack driving force \bar{Y} as discussed in Section 3.

Using the Gauss divergence theorem, the governing equation (strong form) for a cracking solid can be written in the reference (initial) configuration as

$$\begin{cases} \nabla_0 \cdot \mathbf{P} + \mathbf{b}^* = \rho \ddot{\mathbf{u}} & \text{in } \Omega_0 \\ \omega'(d) \bar{Y} + \frac{G_f}{c_\alpha} \left[\frac{1}{b} \alpha'(d) - 2b \Delta_0 d \right] \geq 0 \quad \dot{d} \geq 0 & \text{in } \Omega_0 \end{cases} \quad (2.5a)$$

with natural boundary conditions,

$$\begin{cases} \mathbf{P} \cdot \mathbf{n} = \mathbf{t}^* & \text{on } \partial\Omega_{0,t} \\ \frac{2b}{c_\alpha} \nabla_0 d \cdot \mathbf{n} = 0 & \text{on } \partial\Omega_0 \end{cases} \quad (2.5b)$$

For the nominal stress \mathbf{P} , $\mathbf{P} := \frac{\partial \psi}{\partial \mathbf{F}^T} = \mathbf{S} \mathbf{F}^T$. And the Laplacian of damage defined as: $\Delta_0 d := \frac{\partial^2 d}{\partial X^2} + \frac{\partial^2 d}{\partial Y^2} + \frac{\partial^2 d}{\partial Z^2}$. In addition to the above natural boundary conditions, one also needs to consider Dirichlet boundary conditions with prescribed displacements $\mathbf{u}^*(\mathbf{X})$ for $\mathbf{X} \in \partial\Omega_{0,u}$ and initial conditions: $\mathbf{u}(\mathbf{X}, 0) = \mathbf{u}_0(\mathbf{X})$, and $\dot{\mathbf{u}}(\mathbf{X}, 0) = \mathbf{v}_0(\mathbf{X})$ for the velocity field $\dot{\mathbf{u}}(\mathbf{X}, t) := d\mathbf{u}(\mathbf{X}, t)/dt$. Moreover, the damage is subjected to the damage boundedness condition $0 \leq d \leq 1$.

To complete the model, one needs to (i) furnish a concrete model for the bulk i.e., Section 3.1: $\psi_s(\mathbf{C})$ and particularly its positive/negative parts $\psi_0^{+/-}(\mathbf{C})$; and (ii) specify the crack geometric function $\alpha(d)$ and the degradation function $\omega(d)$. They are the subjects of the next section.

3. Material constitutive model

In this section, we present concrete expressions for the strain energy density, the crack geometric function and the degradation function. First, two Neo-Hookean material laws along with positive/negative decompositions are discussed in Section 3.1: one is the widely used compressible Neo-Hookean material and the other is a model presented in [64]. Second, Section 3.2 outlines the adopted crack geometric and the degradation function taken from the PF-CZM. And finally, Section 3.3 summarizes all major equations of PFM for hyperelastic brittle fracture.

3.1. Neo-Hookean models

In this study, we have considered the following two compressible Neo-Hookean material models:

1. Neo-Hookean-I: a widely used standard Neo-Hookean model [10,95],
2. Neo-Hookean-II: a simplified Neo-Hookean model [64] which has been found suitable for phase field fracture study [78,93].

The undamaged strain energy density ψ_0 , effective stress \bar{S}_{ij} and effective material tangent $\bar{\mathbb{D}}_{ijkl}$ for Neo-Hookean-I/II are summarised using two tables: (a) Table 3 – without any split, and (b) Table 4 – Tang et al.’s volumetric-stretch based split. The volumetric split of Amor et al. [7] can be obtained by considering only the J -dependence part of this split. The (effective and positive/negative) material tangents are needed in the finite element implementation (Section 5.2.1).

For a specific Neo-Hookean model (I or II) and a specific split, one can have two options: a variationally consistent model and a

Table 3

Neo-Hookean material models without any split. $J := \det \mathbf{F}$, $\eta := 2\nu_0/(1 - 2\nu_0)$; λ_0 and μ_0 are Lamé’s constants of elasticity. See (C.8a) for explicit expressions for C_{ijkl} . Follow Appendix B for plane stress implementation.

Model	ψ_0	\bar{S}_{ij}	$\bar{\mathbb{D}}_{ijkl}$
<hr/>			
Neo-Hookean-I			
Neo-Hookean-II	$\underbrace{\frac{\mu_0}{2} (\text{tr}(\mathbf{C}) - 3) - \mu_0 \log J}_{\psi_d} + \underbrace{\frac{\lambda_0}{2} (\log J)^2}_{\psi_v}$ $\lambda_0 \log J C_{ij}^{-1} + \mu_0 (\delta_{ij} - C_{ij}^{-1})$ $\lambda_0 C_{ij}^{-1} C_{kl}^{-1} - 2(\mu_0 - \lambda_0 \log J) C_{ijkl}$	$\mu_0 J^{-\eta} (\eta C_{ij}^{-1} C_{kl}^{-1} - 2C_{ijkl})$ $\mu_0 (\delta_{ij} - J^{-\eta} C_{ij}^{-1})$	

Table 4

Volumetric-stretching split of Neo-Hookean material models. NH-I/II represents Neo-Hookean-I/II, respectively and $[+]/[-]$ denote the positive/negative part of the corresponding variable. β_n^i represents i -th element of n -th eigenvector β_n whereas p_n represents the n -th eigenvalue. See (C.8a)–(C.8d) for C_{ijkl} , Q_{ijkl} and R_{ijkl} , respectively.

NH-I	[+]	[-]
ψ_0		
\bar{S}_{ij}	$\frac{\mu_0}{2} \sum_{n=1}^3 (p_n - 1 - \log p_n) _{p_n > 1} + \frac{\lambda_0}{2} (\log J)^2 _{J > 1}$	$\frac{\mu_0}{2} \sum_{n=1}^3 (p_n - 1 - \log p_n) _{p_n < 1} + \frac{\lambda_0}{2} (\log J)^2 _{J < 1}$
\bar{D}_{ijkl}	$\mu_0 \sum_{n=1}^3 (1 - p_n^{-1}) \beta_n^i \beta_n^j _{p_n > 1} + \lambda_0 \log J C_{ij}^{-1} _{J > 1}$	$\mu_0 \sum_{n=1}^3 (1 - p_n^{-1}) \beta_n^i \beta_n^j _{p_n < 1} + \lambda_0 \log J C_{ij}^{-1} _{J < 1}$
		$2\mu_0 \sum_{n=1}^3 Q_{n,ijkl} _{p_n > 1} + \lambda_0 (C_{ij}^{-1} C_{kl}^{-1} + 2 \log J C_{ijkl}) _{J > 1}$
$2\mu_0 \sum_{n=1}^3 Q_{n,ijkl} _{p_n < 1} + \lambda_0 (C_{ij}^{-1} C_{kl}^{-1} + 2 \log J C_{ijkl}) _{J < 1}$		
NH-II	[+]	[-]
ψ_0		
\bar{S}_{ij}	$\frac{\mu_0}{2} \sum_{n=1}^3 (p_n - 1) _{p_n > 1} + \frac{\mu_0}{\eta} (J^{-\eta} - 1) _{J > 1}$	$\frac{\mu_0}{2} \sum_{n=1}^3 (p_n - 1) _{p_n < 1} + \frac{\mu_0}{\eta} (J^{-\eta} - 1) _{J < 1}$
\bar{D}_{ijkl}	$\mu_0 \sum_{n=1}^3 \beta_n^i \beta_n^j _{p_n > 1} - \mu_0 J^{-\eta} C_{ij}^{-1} _{J > 1}$	$\mu_0 \sum_{n=1}^3 \beta_n^i \beta_n^j _{p_n < 1} - \mu_0 J^{-\eta} C_{ij}^{-1} _{J < 1}$
		$2\mu_0 \sum_{n=1}^3 R_{n,ijkl} _{p_n > 1} + \mu_0 J^{-\eta} (\eta C_{ij}^{-1} C_{kl}^{-1} - 2 C_{ijkl}) _{J > 1}$
$2\mu_0 \sum_{n=1}^3 R_{n,ijkl} _{p_n < 1} + \mu_0 J^{-\eta} (\eta C_{ij}^{-1} C_{kl}^{-1} - 2 C_{ijkl}) _{J < 1}$		

hybrid model (**Table 5**). A hybrid formulation for hyperelastic solids is not new as Raina and Miehe [78] have presented a hybrid formulation with a Rankine type crack driving force applicable for anisotropic hyperelastic fracture.

Once the second Piola-Kirchoff stress has been found, the nominal stress P and Cauchy stress σ (also known as true stress) can be computed as

$$P := SF^T, \quad \sigma := J^{-1}FP = J^{-1}FSF^T \quad (3.1)$$

3.2. Phase-field regularised cohesive zone model (PF-CZM)

In PFMs, the geometric crack function $\alpha(d)$ and energetic degradation function $\omega(d)$ constitute the material constitutive relation for the damage behaviour. In the PF-CZM, $\alpha(d)$ is a quadratic function which allows an elastic domain before crack initiation and finite width of the damage band; while $\omega(d)$ is a rational function with multiple parameters allowing to model a variety of material softening [85].

Table 5

Effective crack driving force, second Piola-Kirchoff stress and material tangent for variationally consistent and hybrid formulation for hyperelasticity.

	Variationally consistent	Hybrid
\bar{Y}	ψ_0^+	ψ_0^+
\bar{S}	$\omega(d)\bar{S}^+ + \bar{S}^-$	$\omega(d)\bar{S}$
\bar{D}	$\omega(d)\bar{D}^+ + \bar{D}^-$	$\omega(d)\bar{D}$

Table 6

A summary of hyperelastic fracture PFM considered in this study: variationally consistent anisotropic models only. Hybrid models can be obtained with the stress $\mathbf{S} = \omega(d)\bar{\mathbf{S}}f_{le}$ given by Eq. (4.8). Refer to Table 4 for ψ_0^+ and $\bar{\mathbf{S}}^{+/-}$ if Tang et al.'s split is used.

	AT1	AT2	PF-CZM
$\omega(d)$	$(1-d)^2$	$(1-d)^2$	$\frac{(1-d)^p}{(1-d)^p + Q(d)}$
$\alpha(d)$	d	d^2	$2d - d^2$
\bar{Y}	ψ_0^+	ψ_0^+	ψ_0^+
\mathbf{S}	$\omega(d)\bar{\mathbf{S}}^+ + \bar{\mathbf{S}}^-$	$\omega(d)\bar{\mathbf{S}}^+ + \bar{\mathbf{S}}^-$	$\omega(d)\bar{\mathbf{S}}^+ + \bar{\mathbf{S}}^-$
b	$\frac{3}{8} \cdot \frac{E_0 G_f}{f_{le}^2}$	$(0.095 + 0.00132 \epsilon_e - 4 \times 10^{-5} \epsilon_e^2) \cdot \frac{E_0 G_f}{f_{le}^2}$	a small number

$$\alpha(d) = 2d - d^2, \quad \omega(d) = \frac{(1-d)^p}{(1-d)^p + Q(d)} \quad (3.2a)$$

$$\alpha'(d) = 2 - 2d \quad \omega'(d) = \frac{-p(1-d)^{p-1}Q(d) - (1-d)^pQ'(d)}{[(1-d)^p + Q(d)]^2} \quad (3.2b)$$

$$Q(d) = a_1 d + a_1 a_2 d^2 + a_1 a_2 a_3 d^3 \quad Q'(d) = a_1 + 2a_1 a_2 d + 3a_1 a_2 a_3 d^2 \quad (3.2c)$$

where $c_\alpha := 4 \int_0^1 \sqrt{\alpha(\bar{x})} d\bar{x} = \pi$; coefficient $a_1 = \frac{4}{\pi} \cdot \frac{l_{ch}}{b}$ with $l_{ch} := E_0 G_f / f_{le}^2$ is Griffith's or Irwin's internal length; f_{le} is an equivalent tensile strength – related to f_t – to be discussed in Section 4.2. We have provided expressions for $\alpha'(d)$, $\omega'(d)$ and $Q'(d)$ as they are needed in Section 4.

For small strain quasi-brittle fracture, Wu [85] derived an exact localized solution for a softening bar. From that solution, the exponent p , and coefficients a_2 , a_3 are determined for a given softening law. For instance, for a linear softening law, the parameters (p , a_2 , a_3) are: $p = 2$, $a_2 = -0.5$ and $a_3 = 0.0$ [85].

We are unable to find the exact localized solution for a hyperelastic softening bar (because the equations are highly nonlinear). So, we use $p = 2$, $a_2 = -0.5$ and $a_3 = 0.0$ from the small strain PF-CZM for a linear softening to model hyperelastic brittle fracture. Even though we do not exclude the possibility of using other values for parameters (p , a_2 , a_3), we demonstrate in Section 6 that the considered values perform well.

3.3. A summary

In summary, the equations for a PFM for hyperelastic brittle fracture are: governing partial differential equations in Eq. (2.5) with details for the bulk material model in Table 4 and crack geometric and degradation function in Table 6 (only for variationally consistent formulations). We refer to Section 4.2 for the derivation of the length scale formula (last row of Table 6).

Remark 3.1. There are some other models with $\alpha(d) = d^2$ and $\omega(d)$ that is a cubic, a quartic [47] and a mixed quadratic-cubic degradation function [14]. The model with a mixed quadratic-cubic function also possess a (nearly) elastic domain similar to the AT1 and PF-CZM. Loew et al. [51] compared the AT2 with these models. Even though they all can capture experiments, the material parameters G_f and b vary from models to models. We think that the fracture toughness should be independent of the employed degradation function.□

We actually consider 24 models: 3 PFMs (AT1, AT2, PF-CZM), 2 bulk materials (Neo-Hookean I and II), 2 splits and 2 compression/tension asymmetry formulations (variationally consistent and hybrid).

4. Homogeneous solutions and formula to compute the length scale

In this section, one of our main contributions, we present a formula relating the length scale to the tensile strength of the material, similar to the well known $b = (27/256)(E_0 G_f / f_t^2)$ for the small strain AT2 model. This is significant as it is widely accepted that the length scale must be considered as a material parameter, rather than any small positive number, for the AT1/2 [74,68].

To this end, we consider a one dimensional bar subjected to a monotonically increasing tensile strain (a traction bar). Furthermore, no body force and acceleration are considered. Importantly, it suffices to consider only a homogeneous damage state i.e., the damage is uniform in the bar. The procedure is to calculate the stress field in the bar, find its maximum and equate this maximum stress to the material tensile strength, and a relation between b and E_0 , G_f and f_t will pop out.

We plan this section as follows. The homogeneous solutions for the damage and stress field are provided in Section 4.1. Then, we derive the relation between b and some material properties in Section 4.2.

4.1. Homogeneous damage and stress field

The governing equations in Eq. (2.5) are now simplified as

$$\begin{aligned} P_{,X} &= 0 \\ \omega'(d)\bar{Y} + \frac{G_f}{bc\alpha}\alpha'(d) &= 0 \end{aligned} \quad (3.2d)$$

where $\bar{Y} = \psi_0$ as no split is needed in this case; $\omega'(d)$ and $\alpha'(d)$ are given by

$$\text{AT1: } \omega'(d) = -2(1-d), \quad \alpha'(d) = 1 \quad (4.2\text{a})$$

$$\text{AT2: } \omega'(d) = -2(1-d), \quad \alpha'(d) = 2d \quad (4.2\text{b})$$

$$\text{PF - CZM : } \omega'(d) = \frac{4a_1(d-1)}{(2a_1d-4d-a_1d^2+2d^2+2)^2}, \quad \alpha'(d) = 2-2d \quad (4.2\text{c})$$

The second equation of Eq. (4.1) plus Eq. (4.2) result in the following homogeneous damage field d_{hom} ,

$$\text{AT1: } d_{\text{hom}} = \frac{1}{2\bar{Y}} \left(2\bar{Y} - \frac{G_f}{c_\alpha b} \right), \quad \text{with } c_\alpha = 8/3 \quad (4.3\text{a})$$

$$\text{AT2: } d_{\text{hom}} = \bar{Y} \left(\bar{Y} + \frac{G_f}{c_\alpha b} \right)^{-1}, \quad \text{with } c_\alpha = 2 \quad (4.3\text{b})$$

$$\text{PF - CZM : } d_{\text{hom}} = 1 - \sqrt{\frac{A_0a_1 - \sqrt{2A_0a_1\bar{Y}}}{A_0(a_1-2)}}, \quad \text{with } A_0 = \frac{G_f}{c_\alpha b}, \quad a_1 = \frac{4}{\pi} \cdot \frac{l_{\text{ch}}}{b} \quad (4.3\text{c})$$

which shows that the AT2 does not have an elastic domain but the AT1 and PF-CZM do. The elastic domain is defined by $\bar{Y} \leq \bar{Y}_{\text{th}}$, where \bar{Y}_{th} denotes a damage threshold given by

$$\text{AT1: } \bar{Y}_{\text{th}} = \frac{G_f}{2c_\alpha b} = \frac{3G_f}{16b} \quad (4.4\text{a})$$

$$\text{PF - CZM: } \bar{Y}_{\text{th}} = \frac{2G_f}{c_\alpha ba_1} = \frac{G_f}{2l_{\text{ch}}} = \frac{f_{\text{te}}^2}{2E_0} \quad (4.4\text{b})$$

The damage threshold \bar{Y}_{th} for the PF-CZM is not a function of the length scale and thus it provides length-scale insensitive response. An attractive feature of the AT2 is that it automatically provides an admissible damage field i.e., $0 \leq d \leq 1$. For the AT1 and PF-CZM, one needs to enforce the condition $0 \leq d \leq 1$. Eq. (4.4a) is the key equation to derive a formula for the length scale as discussed in Section 4.2.

Next, we compute the stress and strain. For infinitesimal strain ϵ_x , the deformation gradient F , the right Cauchy-Green deformation tensor C and Green-Lagrange strain E can be written as,

$$F = \begin{bmatrix} 1 + \epsilon_x & 0 \\ 0 & 1 \end{bmatrix}, \quad C = \begin{bmatrix} (1 + \epsilon_x)^2 & 0 \\ 0 & 1 \end{bmatrix}, \quad E = \begin{bmatrix} \epsilon_x + 0.5 \epsilon_x^2 & 0 \\ 0 & 0 \end{bmatrix} \quad (4.5)$$

Following Table 3 and assuming a plane strain state, the effective strain energy density and effective stress are provided in Table 7. The second Piola-Kirchoff stress S_x , the nominal stress P_x and Cauchy stress σ_x are computed using Eq. (3.1) as

$$S_x = \omega(d_{\text{hom}})\bar{S}_x, \quad P_x = (1 + \epsilon_x)S_x = \omega(d_{\text{hom}})(1 + \epsilon_x)\bar{S}_x \quad \sigma_x = J^{-1}(1 + \epsilon_x)P_x = P_x \quad (4.6)$$

with degradation function $\omega(d_{\text{hom}})$ as defined in Table 1 for AT1/2 and Eq. (3.2) for PF-CZM.

4.2. Damage threshold and peak stress

For the AT1/2 for elastic brittle fracture, it is widely accepted that the length scale b should be considered as a material parameter [74,68] calculated using the formulas given in Table 1. These formulas were obtained by calculating the maximum homogeneous stress and equating it with the maximum stress the material can sustain. Such length scales are inversely proportional to the square of the material maximum stress and for $b \rightarrow 0$, the predicted maximum stress approaches infinity, consistent with linear elastic fracture mechanics [28].

Herein, we derive relations for the AT1/2 for both Neo-Hookean materials. We derive the equations particularly for Neo-Hookean-I with a null Poisson's ratio (to simplify the calculations), but keeping in mind that, Neo-Hookean-II converges to Neo-Hookean-I when $\nu_0 \rightarrow 0$.

Table 7

One dimensional analytical solution for different materials. For linear elasticity, the stress measure is $\bar{\sigma}_x$.

	ψ_0	\bar{S}_x
Linear elasticity:	$\left(\frac{\lambda_0}{2} + \mu_0\right) \epsilon_x^2$	$(\lambda_0 + 2\mu_0) \epsilon_x$
Neo-Hookean-I:	$\frac{\mu_0}{2}(\epsilon_x^2 + 2\epsilon_x - 2\log(1 + \epsilon_x)) + \frac{\lambda_0}{2}(\log(1 + \epsilon_x))^2$	$\frac{\lambda_0 \log(1 + \epsilon_x) + \mu_0(\epsilon_x^2 + 2\epsilon_x)}{(1 + \epsilon_x)^2}$
Neo-Hookean-II:	$\frac{\mu_0}{2}(\epsilon_x^2 + 2\epsilon_x) + \frac{\mu_0}{\eta}((1 + \epsilon_x)^{-\eta} - 1)$	$\mu_0(1 - (1 + \epsilon_x)^{-\eta-2})$

4.2.1. PFM_s with an elastic domain (AT1 and PF-CZM)

Our derivation is based on this stress-strain relationship: a linear elastic portion up to the peak (which is equal to f_t) followed by a vertical stress drop. Damage initiation occurs at the peak stress. So, from Eq. (4.4) one can write

$$\bar{Y}_{th} = \frac{3G_f}{16b_{AT1}} \rightarrow \psi_0(f_t) = \frac{3G_f}{16b_{AT1}} \rightarrow b_{AT1} = \frac{3}{8} \cdot \frac{E_0 G_f}{f_{te}^2} \quad (4.7)$$

The formula for b is similar to the one for linear elasticity, as presented in Table 1, except the fact that f_{te} , not f_t , is used. In Eq. (4.7), f_{te} , the equivalent tensile strength, is given by

$$f_{te} := \sqrt{2E_0\psi_0(f_t)} \quad (4.8)$$

which is valid for $\nu_0 = 0.0$. For Neo-Hookean materials, $f_{te} > f_t$. What remains is to find the expression for $\psi_0(f_t)$.

For Neo-Hookean-I/II, the undamaged strain energy and effective stress $\bar{\sigma}_x$ given in Table 7, are simplified as (with $\nu_0 = 0$, $\lambda_0 = 0$ and $\mu_0 = \frac{E_0}{2}$)

$$\psi_0 = \frac{E_0}{4}(\epsilon_x^2 + 2\epsilon_x - 2\log(1 + \epsilon_x)) \quad (4.9a)$$

$$\bar{\sigma}_x = \frac{E_0}{2} \frac{\epsilon_x^2 + 2\epsilon_x}{(1 + \epsilon_x)^2} \rightarrow \bar{\sigma}_x = \frac{E_0}{2} \left(\frac{\epsilon_x^2 + 2\epsilon_x}{1 + \epsilon_x} \right) \rightarrow \epsilon_x = \frac{\bar{\sigma}_x}{E_0} \left(1 + \sqrt{1 + \left(\frac{E_0}{\bar{\sigma}_x} \right)^2} \right) - 1 \quad (4.9b)$$

where we used Eq. (4.6) to convert from $\bar{\sigma}_x$ to $\bar{\sigma}_x$. The last equation in Eq. (4.9) allows to compute the failure (or critical) strain $\epsilon_{cr} := \epsilon_x(f_t)$.

More importantly, Eq. (4.9) allows us to write ψ_0 explicitly in terms of $\bar{\sigma}_x$ as,

$$\psi_0(\bar{\sigma}_x) = \frac{\bar{\sigma}_x^2}{2E_0} \left(1 + \sqrt{1 + \left(\frac{E_0}{\bar{\sigma}_x} \right)^2} \right) - \frac{E_0}{2} \log \left[\frac{\bar{\sigma}_x}{E_0} \left(1 + \sqrt{1 + \left(\frac{E_0}{\bar{\sigma}_x} \right)^2} \right) \right] \quad (4.10)$$

which is used to compute $\psi_0(f_t)$ required for f_{te} .

Moreover, one can relate material tensile strength f_t with f_{te} explicitly using Eq. (4.8) and (4.9)

$$f_t = \frac{E_0}{2} \sqrt{-\gamma} \left(\frac{1}{\gamma} + 1 \right), \quad \text{with } \gamma := \text{Real} \left[\mathcal{W} \left(-2 \left(\frac{f_{te}}{E_0} \right)^2 - 1 - \pi i \right) \right] \quad (4.11)$$

where $\mathcal{W}(\cdot)$ represents the Wright omega function which can be computed using `wrightOmega` in MATLAB.

4.2.2. PFM_s without an elastic domain (AT2)

Deriving a similar equation for the length scale parameter of the AT2 is difficult due to lack of an elastic domain. We find the length scale for a given f_t by setting the maximum stress in the bar equal to the tensile strength. That means solving the following coupled equations for $\{b_{AT2}, \epsilon_x\}$ numerically (we used the `vpasolve` function of Matlab),

$$\frac{d^{(\omega(d_{hom})\bar{\sigma}_x)} \epsilon_x}{d} = 0 \quad (4.12a)$$

$$\omega(d_{hom})\bar{\sigma}_x = f_t \quad (4.12b)$$

with $\omega(d_{hom}) := (1 - d_{hom})^2 = \left(\frac{G_f}{G_f + 2\psi_0 b_{AT2}} \right)^2$ using (4.3b) for d_{hom} , and Eq. (4.9) for ψ_0 and $\bar{\sigma}_x$. An approximate expression for b_{AT2} is obtained using a least square fit as,

$$b_{AT2} = \left(0.095 + 0.00132 \epsilon_e - 4 \times 10^{-5} \epsilon_e^2 \right) \cdot \frac{E_0 G_f}{f_{te}^2} \quad (4.13)$$

with $\epsilon_e := \frac{f_{te}}{E_0}$ where f_{te} is computed using Eq. (4.8) and applicable for wide range of $\epsilon_e \in [0, 30]$ with error <5%.

The homogeneous solutions are only valid prior to damage localization (and it is possible for this simplified geometry of a bar). After that instance, damage localises, and the corresponding analytical solutions are very difficult to obtain. We resort to numerical methods to be presented in the next section to get damage localization solutions for any geometries.

5. Finite element implementation

This section presents the finite element (FE) implementation of the phase field models introduced in Section 2 and 3, summarized in Table 6, in a standard FE code. Our implementation is generic as it includes the AT1/2 and the PF-CZM with both Neo-Hookean materials. Also, it includes both the variationally consistent anisotropic formulation and the hybrid one. Appendix A presents the FEniCS implementation. We start with the FE approximations of the displacement and damage field and the resulting discrete equations in Section 5.1. Solution algorithms to solve these discrete equations are then provided in Section 5.2.

5.1. Finite element equations

In the finite element method, the displacement field $\mathbf{u}(\mathbf{X})$ and damage field $d(\mathbf{X})$ are approximated using the nodal displacements \mathbf{a} and nodal damage $\bar{\mathbf{a}}$ with corresponding interpolating functions $\mathbf{N}_I(\mathbf{X})$ and $\bar{\mathbf{N}}_I(\mathbf{X})$, respectively. They are written as

$$\mathbf{u}(\mathbf{X}) = \sum_I \mathbf{N}_I(\mathbf{X}) \mathbf{a}_I = \mathbf{Na} \quad (5.1a)$$

$$d(\mathbf{X}) = \sum_I \bar{\mathbf{N}}_I(\mathbf{X}) \bar{\mathbf{a}}_I = \bar{\mathbf{N}}\bar{\mathbf{a}} \quad (5.1b)$$

which results in the following expressions for the gradients (with respect to \mathbf{X}) of the displacement and damage field

$$\nabla_0 \mathbf{u}(\mathbf{X}) = \sum_I B_I \mathbf{a}_I = \mathbf{B}\mathbf{a} \quad (5.2a)$$

$$\nabla_0 d(\mathbf{X}) = \sum_I B_I(\mathbf{X}) \bar{\mathbf{a}}_I = \mathbf{B}\bar{\mathbf{a}} \quad (5.2b)$$

Now, the variational formulation given in Eq. (2.4) can be written as

$$\mathbf{r}^u := \mathbf{f}^{ext} - \int_{\Omega_0} \mathbf{B}_0^T \mathbf{S} dV - \mathbf{M}\ddot{\mathbf{a}} = \mathbf{0} \quad (5.3a)$$

$$\mathbf{r}^d := - \int_{\Omega_0} \left[\bar{\mathbf{N}}^T \left(\omega'(\bar{\mathbf{a}}) \bar{Y} + \alpha'(\bar{\mathbf{a}}) \frac{G_f}{c_\alpha b} \right) + \frac{2b}{c_\alpha} G_f \bar{\mathbf{B}}^T \nabla_0 d \right] dV \leq \mathbf{0} \quad (5.3b)$$

with modified B-matrix $\mathbf{B}_0 = \mathbf{B}\mathbf{F}^T$, nodal acceleration $\ddot{\mathbf{a}} := d^2\mathbf{a}/dt^2$, consistent mass matrix $\mathbf{M} := \int_{\Omega_0} \mathbf{N}^T \rho \mathbf{N} dV$ and external force vector $\mathbf{f}^{ext} := \int_{\Omega_0} \mathbf{b}^* dV + \int_{\Omega_{0,t}} \mathbf{t}^* dA$. Section D provides expressions for \mathbf{N} , \mathbf{B}_0 and $\bar{\mathbf{B}}$.

Remark 5.1. For numerical purposes, it is customary to introduce a residual strength κ to the formulation by modifying the degradation function as

$$\omega(d) = (1 - \kappa)\omega_0(d) + \kappa \quad (5.4)$$

where $\omega_0(d)$ are given in Table 6; for example $\omega_0(d) = (1 - d)^2$ for the AT1/2. Note that this form is better than $\omega_0(d) + \kappa$, commonly used in PFMs for small strain solids, for κ in the range 10^{-3} to 10^{-1} . We discuss the role of this parameter in Section 6.5. \square

5.2. Solution procedures

To solve Eq. (5.3), we adopt the alternating minimization (AM) or staggered solver, proposed in Bourdin et al. [15]. This AM solver is more robust and flexible than a monolithic solver and keep in mind that we are solving static fracture problems not dynamics fracture. In the AM solver, we solve the displacement sub-problem, Eq. (5.3a), for the nodal displacements with a fixed damage field. Next, we solve the damage sub-problem, Eq. (5.3b), for the nodal damage with the updated nodal displacements. The process is repeated until convergence. See Wu et al. [88] for detail.

We have encountered numerical non convergence for hyperelastic brittle fracture simulations, particularly, in the softening regime. Previous studies have reported the same issue and tried to resolve it using minuscule displacement increments in the order of 10^{-6} mm [64] and/or using a large residual strength κ [82,94,84]. To deal with this convergence problem, we have tried the following solution algorithms:

- The standard AM solver where the displacement and damage sub-problems are solved multiple times until convergence. This solver allows large displacement increments;
- A single-iteration AM solver developed by Miehe et al. [66] where the displacement and damage sub-problems are solved only one time per load step. This solver demands tiny displacement increments;
- Within either the standard AM or the single-iteration AM, the damage sub-problem can be enhanced with a viscous regularization term;
- An implicit-explicit solver where the state from beginning to crack initiation is solved using any of the above three solvers. The state from crack propagation to final failure is solved using an explicit dynamics solver for Eq. (5.3).

The attributes of these algorithms are given in Table 8 keeping in mind that they are simply general guidelines for the selection of a solution algorithm.

5.2.1. Displacement sub-problem

Only when the implicit-explicit solver is used and we are dealing with crack propagation, then inertia effect is included in the displacement sub-problem, Eq. (5.3a). In that case, we adopt the explicit Newmark solver. Other than that, inertial is excluded and we use the standard Newton-Raphson solver for the displacement sub-problem. This section discusses these two solvers.

Table 8

Qualitative assessment of solvers. Viscous AM refers to the single-iteration AM with a viscous regularization term in the damage sub-problem. In the implicit-explicit solver, only one AM iteration is used for sake of implementation. By complexity, we meant the implementation effort.

	Std (multiple-iter.) AM solver	Single-iteration AM	Viscous AM	Implicit-Explicit
Efficiency	☺	☺☺	☺☺	☺☺☺
Robustness	☺	☺	☺☺	☺☺☺
Complexity	☺☺	☺	☺	☺☺☺

Implicit algorithm. Using the Newton-Raphson solver, we solve the following system of linear equations for the incremental nodal displacement $\delta \mathbf{a}$

$$\left[\underbrace{\int_{\Omega_0} \mathbf{B}_0^T \mathbf{D} \mathbf{B}_0 dV}_{\text{material stiffness } \mathbf{K}_{\text{mat}}} + \mathbf{I} \underbrace{\int_{\Omega_0} \mathbf{B}_I^T [\mathbf{S}] \mathbf{B}_I dV}_{\text{geometric stiffness } \mathbf{K}_{\text{geo}}} \right] \delta \mathbf{a}_I = \mathbf{f}_I^{\text{ext}} - \mathbf{f}_I^{\text{int}} \quad (5.1)$$

with the internal force vector $\mathbf{f}_I^{\text{int}} := \int_{\Omega_0} \mathbf{B}_0^T \mathbf{S} dV$, and \mathbf{I} is a unit matrix whose dimension equals n_{dim} . The material stiffness matrix \mathbf{K}_{mat} is identical to stiffness matrix corresponding to infinitesimal deformation problems except the modified B-matrix \mathbf{B}_0 as shown in Eq. (D.1). The second part of the stiffness matrix is due to nonlinear strain-displacement relations, usually called as geometric stiffness \mathbf{K}_{geo} . Section D gives the expression for the geometric stiffness matrix. In the geometric stiffness, the second Piola-Kirchoff stress is a matrix, and we used $[\mathbf{S}]$ to differentiate it from the stress vector \mathbf{S} . Note that Eq. (5.5) is valid only if the load does not depend on the deformation. As we only used a displacement control, it is the case.

Explicit dynamic algorithm. We adopt the explicit Newmark's algorithm as discussed in Nguyen and Wu [69]. Given a time step size Δt , the nodal displacement \mathbf{a}_{n+1} , velocity $\dot{\mathbf{a}}_{n+1}$ and acceleration $\ddot{\mathbf{a}}_{n+1}$ at the instant t_{n+1} are approximated as,

$$\mathbf{a}_{n+1} = \mathbf{a}_n + \Delta t \dot{\mathbf{a}}_n + \frac{(\Delta t)^2}{2} \ddot{\mathbf{a}}_n \quad (5.6a)$$

$$\ddot{\mathbf{a}}_{n+1} = \bar{\mathbf{M}}^{-1} \left[\mathbf{f}_{n+1}^{\text{ext}} - \int_{\Omega_0} \mathbf{B}_0^T \mathbf{S} dV \right] \quad \text{with} \quad \mathbf{S} = \mathbf{S} \left(\mathbf{a}_{n+1}, \dot{\mathbf{a}}_n \right) \left(\text{see 3.1} \right) \quad (5.6b)$$

$$\dot{\mathbf{a}}_{n+1} = \dot{\mathbf{a}}_n + \Delta t [(1 - \gamma) \ddot{\mathbf{a}}_n + \gamma \ddot{\mathbf{a}}_{n+1}] \quad \text{with} \quad \gamma = 0.5 \quad (5.6c)$$

For stability, the time step is chosen to satisfy the following Courant-Friedrichs-Lowy condition

$$\Delta t \leq \Delta t_{\text{crit}} := \alpha \frac{h}{C_s} \quad (5.7)$$

where h denotes the smallest element size, C_s is the shear wave speed in the material and $0 < \alpha < 1$ is a safety factor. As the time step size Δt is small, one only needs to carry out one AM iteration.

As we are solving static problems using an explicit dynamics formulation, it is a good practice to adopt some damping. We use a local damping formulation, well documented in [43], in which the sign of the damping force is decided based on the sign of nodal velocity \dot{a}_{il} and the sign of $(f_{il}^{\text{ext}} - f_{il}^{\text{int}})$ for each dof. Without external forces, e.g. displacement controlled simulations, the internal force vector is equivalently modified for each dof a_{il} to account for damping,

$$f_{il}^{\text{int,damp}} := \left(1 + \text{sign} \left(\frac{\dot{a}_{il}}{f_{il}^{\text{int}}} \right) \zeta \right) f_{il}^{\text{int}} \quad (5.8)$$

with a damping factor ζ and $i = \{x, y, z\}$ represents the components of a vector; $\text{sign}(p)$ returns ± 1 based on whether $p > 0$ or $p < 0$, respectively.

5.2.2. Damage sub-problem

Miehe et al. [66] added a viscous regularization term to the damage sub-problem to enhance the robustness of phase field simulations. We briefly recall this formulation herein. The surface energy functional is now written as,

$$\Psi_c = \int_B [G_f \gamma(d; \nabla_0 d) + \xi \dot{d}] dV \quad (5.9)$$

with a artificial viscosity parameter ξ . Considering a backward Euler approximation, \dot{d} can be written as,

$$\dot{d} = \frac{d - d_{\text{old}}}{\Delta t} \quad (5.10)$$

Table 9

Material parameters and characteristics for all simulations.

Parameter	Section 6.1	Section 6.2	Section 6.3	Section 6.4	Section 6.5
Young's modulus [MPa]	1.0	210×10^3	14.5	0.5887	6.5
Poisson's ratio [-]	0.0	0.3	0.45	0.45	0.45
f_{te} [MPa]	0.57	2445	20	0.65	20
Fracture energy [N/mm]	15 – 35	2.7	2.4	2.67	15
Internal length [mm]	46 – 107	0.095	0.087	3.72	0.24
Fracture mode	mode I	mode I/mixed-mode	mode I	mode I	mixed-mode
Experiments	n/a	n/a	n/a	yes	yes
State	Plane stress	Plane strain	Plane strain	Plane strain	Plane stress
Solver	single-step AM	multi-step AM	single-step AM	imp-exp	imp-exp

with last converged damage value d_{old} and pseudo step size Δt . The FE equation for damage sub-problem Eq. (5.3b) can be modified as,

$$\mathbf{r}^d := - \int_{\Omega_0} \left[\bar{\mathbf{N}}^T \left(\omega'(\bar{\mathbf{a}}) \bar{Y} + \alpha'(\bar{\mathbf{a}}) \frac{G_f}{c_\alpha b} \right) + \frac{2b}{c_\alpha} G_f \bar{\mathbf{B}}^T \nabla_0 d + \xi \bar{\mathbf{N}}^T \bar{\mathbf{N}} \left(\frac{\bar{\mathbf{a}} - \bar{\mathbf{a}}_{old}}{\Delta t} \right) \right] dV \leq \mathbf{0} \quad (5.11)$$

with $\bar{\mathbf{a}}_{old}$ being the converged nodal damage vector. Notice that the case $\xi = 0$ results in the standard damage sub-problem.

Solving the damage sub-problem is more involved as one needs to handle the damage boundedness $0 \leq d \leq 1$ and irreversibility conditions $\dot{d} \geq 0$. The damage problem is actually an optimization problem bounded by the following conditions [6]

$$0 \leq \bar{a}_{I,n} \leq \bar{a}_{I,n+1} \leq 1 \quad \forall I = 1, 2, \dots \quad (5.12)$$

which can be solved by an appropriate solver, e.g., the quadratic optimisation solver included in the Matlab Optimization Toolbox as in Amor et al. [7]. We use the reduced-space active set Newton method [11]. The tangent matrix \mathbf{K}_{dd} is given by

$$\mathbf{K}_{dd} := \int_B \left[\left(\omega'' \bar{Y} + \alpha'' \frac{G_f}{c_\alpha b} \right) \bar{\mathbf{N}}^T \bar{\mathbf{N}} + \frac{2G_f b}{c_\alpha} \bar{\mathbf{B}}^T B + \frac{\xi}{\Delta t} \bar{\mathbf{N}}^T \bar{\mathbf{N}} \right] dV \quad (5.13)$$

where the notation ω'' represents the second derivative of ω with respect to d .

Remark 5.2. Loew et al. [51] demonstrated that using a history variable (representing the maximum ψ_0^+) to deal with $\dot{d} \geq 0$ – a popular technique introduced by Miehe et al. [66] – yields erroneous results for the rate-dependent formulation: damage continues to grow when the strain decreases. \square

6. Numerical examples

To demonstrate the performance of the AT1/2 and particularly the PF-CZM for hyperelastic brittle fracture, the following examples are considered:

1. A uniaxial softening bar (Section 6.1);
2. Single edge notched plate (Section 6.2);
3. Penny shaped pre-cracked specimen (Section 6.3);
4. Symmetric double edge notched specimen (Section 6.4);
5. Mixed mode fracture (Section 6.5);

Notice that all of them are plane strain or plane stress 2D simulations. Although PFM can be used for three dimensional fracture simulations right away, the cost of PFM prevent us from presenting three dimensional examples. The presented examples cover both mode-I and mixed-mode fracture problems. Some are validated against available experiments. Material parameters used for all examples and their characteristics are given in Table 9.

For the PF-CZM, the length scale is chosen such that $b \leq l_{ch}/3$ to ensure the positive definiteness of the stiffness matrix for the damage sub-problem [87]. Sufficiently refined meshes with element size $h \leq b/5$ have to be used to resolve the damage localization [58]. Unless otherwise stated, the hybrid formulation and a linear softening are used.

We present the results for each example in the following way. First, we start with a fixed length scale parameter and a fixed FE mesh, do the simulations and evaluate the crack pattern and the load-displacement response. For cases where experimental findings are available, we compare the numerical crack paths and the global load-displacement response with experiments. Second, we study the mesh convergence of the formulation (with one fixed b and varied h) and the length scale sensitivity of the solution by varying b with a fixed b/h ratio.

In all numerical examples presented in this section, Gmsh [25] was used to generate finite element meshes. Visualization was

realized using Paraview. All the simulations represented herein were carried out using our in-house FE code feFRAC³ [70]. Both three-noded triangular and four-noded quadrilateral elements are used.

6.1. A uniaxial softening bar

This example aims to numerically study the localized solution of a traction bar considered in Section 4 and to verify the formula for the length scale parameter derived in Section 4.2. To this end, we consider a uniaxial bar that is fixed at its left edge and pulled from its right edge (Fig. 2). The material parameters are provided in Table 9 (Neo-Hookean-I material) except a varied material fracture energy $G_f = \{15, 25, 35\}$ N/mm and uniaxial tensile strength $f_t = 0.50$ MPa which leads to Griffith's internal length $l_{ch} = \{45.76, 76.26, 106.77\}$ mm.

From the given f_t of 0.5 MPa, we use Eq. (4.8) to compute the equivalent tensile strength f_{te} : its value is 0.57 MPa. The length scale for the AT1/2 is computed to fit f_t and G_f using Eq. (4.7) and (4.13), respectively: $b_{AT1} = \{17.16, 28.60, 40.09\}$ mm and $b_{AT2} = \{4.28, 7.13, 9.98\}$ mm. A fixed length scale $b = 10$ mm is considered for the PF-CZM.

A single-step AM solver is used with displacement increments $\Delta u^* = 5 \times 10^{-3}$ mm. We had to adopt a viscous regularization for the AT1/2 to avoid numerical divergence. And for this one-dimensional bar, a 2D plane-stress state is assumed.

If the calculations in Section 4.2 were correct, one would expect the peak stress is f_t and a sudden stress drop showing a brittle fracture behaviour. It is indeed the case as shown in Fig. 3a, verifying the developed formula for b . The two models AT1 and PF-CZM behave identically because they both have an elastic domain and the length scale used for the AT1 was chosen to have the peak stress of f_t (similar to the PF-CZM). For the AT2, the damage localizes at a larger displacement which also corresponds to larger failure strain if one follows the solution of Eqs. (4.8) and (4.9b).

Moreover, the AT1/2 represent a pure brittle fracture response in entire range of G_f (Fig. 3c and d), while the PF-CZM shows cohesive behaviour at larger G_f (Fig. 3b). For $G_f = 35$ N/mm, the response of the AT1 is slightly deviated from being brittle due to wider damage band for this case (Fig. 3c).

In summary, uniaxial bar problem is an inexpensive numerical example to test PFMs. Using the PF-CZM, one can observe a brittle or a cohesive fracture by controlling $\frac{l_{ch}}{L}$ – either by varying material parameters (e.g. G_f) or length of the bar.

6.2. Single edge notched plate

The single edge notched plate (SENP) shown in Fig. 4 has become a popular test in the phase field fracture community. Herein, we study the effect of finite deformation and the performance of different Neo-Hookean material models (Table 3) and tension/compression splits of the strain energy. It is also an easy problem to debug the implementation. In Section 6.2.1 we have studied the mode-I fracture w/o any split of strain energy, and mixed-mode fracture is studied in Section 6.2.2 using different split of strain energy of Neo-Hookean materials.

The material parameters are taken from Wu and Nguyen [86] and provided in Table 9. A length scale $b = 0.01$ mm, which is small compared with the internal length scale, is now considered with element size $h = b/5$. A static implicit AM solver is used with incremental displacement of 1×10^{-5} mm. A plane strain state is assumed. No viscous regularization nor residual strength i.e., $\kappa = 0.0$ was used.

6.2.1. Tension test

For the tension test, we have compared the two Neo-Hookean models without strain energy split (because it is not necessary for this problem exhibiting only tensile deformation). The global load-deformation responses using these Neo-Hookean models are quite similar to the linear elastic solution (Fig. 5) and the assumption of small deformation is seen to be justified for this problem. Moreover, both of the Neo-Hookean models, coupled with PF-CZM, are seemed to equally applicable for mode-I fracture problems.

6.2.2. Shear test

For the shear test, we have tested two different strain energy decomposition methods: (1) deviatoric/volumetric decomposition of Amor et al. [7] and, (2) volumetric/stretching decomposition of Tang et al. [82] for the Neo-Hookean-I/II models in provided Table 4. Variationally consistent as well as hybrid formulation have been tried. Among all alternatives, the Neo-Hookean-I with volumetric/stretching decomposition of strain energy gives a smoothly curved crack pattern; Fig. 6(Top). The Neo-Hookean-II behaves quite poorly for this mode-II fracture problem for both strain energy decompositions; Fig. 6(Bottom). Particularly, it shows a straight crack path similar to mode-I when tested with Tang et al.'s split. The load deformation responses are shown in Fig. 7 – which reflects the differences in the corresponding crack patterns quite nicely. Moreover, the load-deformation response using Tang et al.'s split clearly resembles the Miehe's split for linear elasticity [5]. However, Neo-Hookean-II diverges at crack initiation for both type of split when using variational consistent formulation – which reconfirms the inherent inadequacy of its strain energy functional for positive/negative split. One may follow more rigorous mathematical approach to arrive at the same conclusion, which is beyond the scope of current study. In summary, the Neo-Hookean-I with the volumetric/stretching decomposition seems to be a good choice for mode-II (and/or mixed mode) fracture problems while Neo-Hookean-II is not.

For completeness, we have also compared simulation results of Neo-Hookean-I/II with linear elastic solution considering hybrid

³ feFrac stands for finite elements for Fracture which is a C++ code based on the open source jive library at <https://jive.dynaflo.com>.

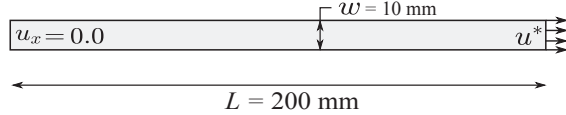


Fig. 2. An uniaxial bar: schematic geometry and loading. Thickness = 1.0 mm.

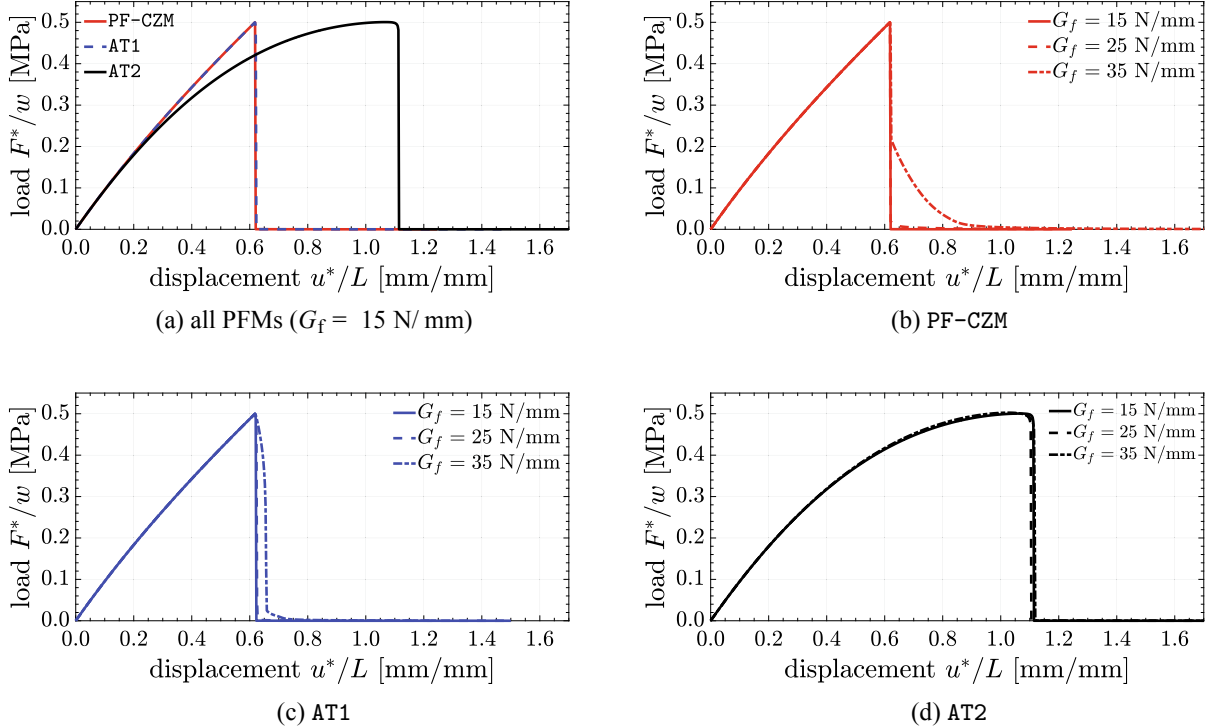


Fig. 3. An uniaxial bar: load-deformation response for $G_f = \{15, 25, 35\} \text{ N/mm}$ and $f_{te} = 0.57 \text{ MPa}$.

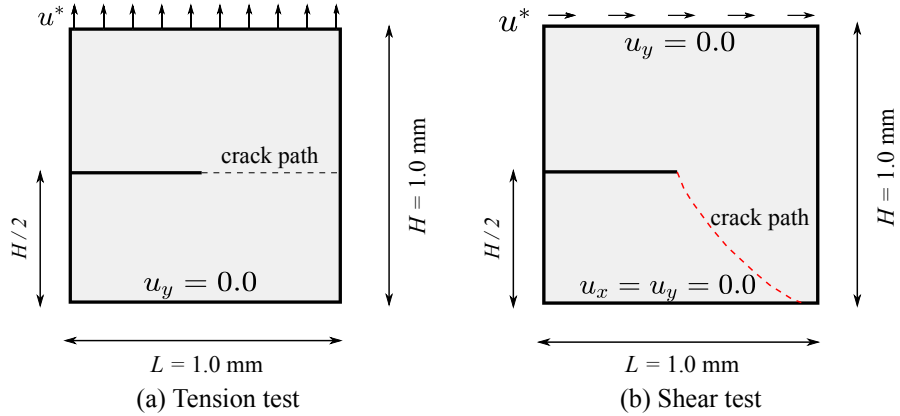


Fig. 4. Single edge notched plate: schematic geometry and loading.

formulation for each case. For convenience, Rankine type crack driving force is used for linear elasticity, Tang et al.'s split for Neo-Hookean-I and Amor et al.'s split for Neo-Hookean-II. The neo-Hookean materials estimate higher failure load as shown in Fig. 8.

Next, we vary the length scale parameter ($b = \{0.01 \text{ mm}, 0.005 \text{ mm}\}$ with element size $h = b/5$) and study the sensitivity of the solution to this parameter. Similar to findings of [86,58] for elastic brittle fracture, PF-CZM also provides length scale insensitive response for hyperelastic fracture (Fig. 9).

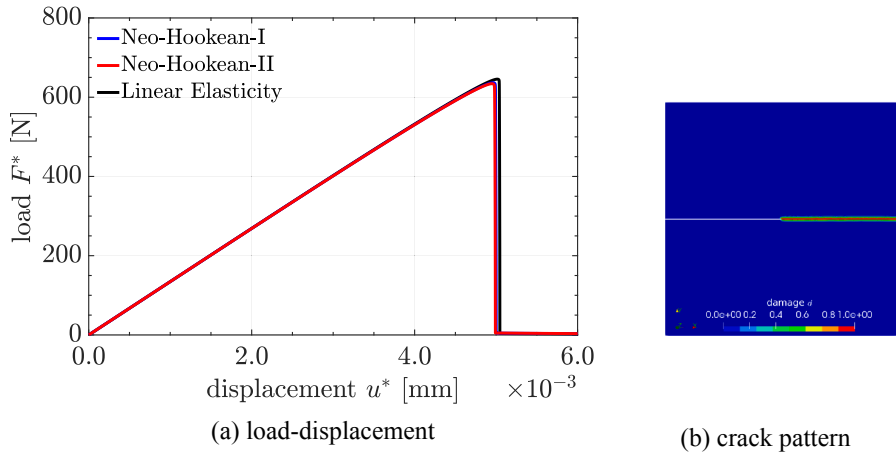


Fig. 5. Single edge notched plate in tension.

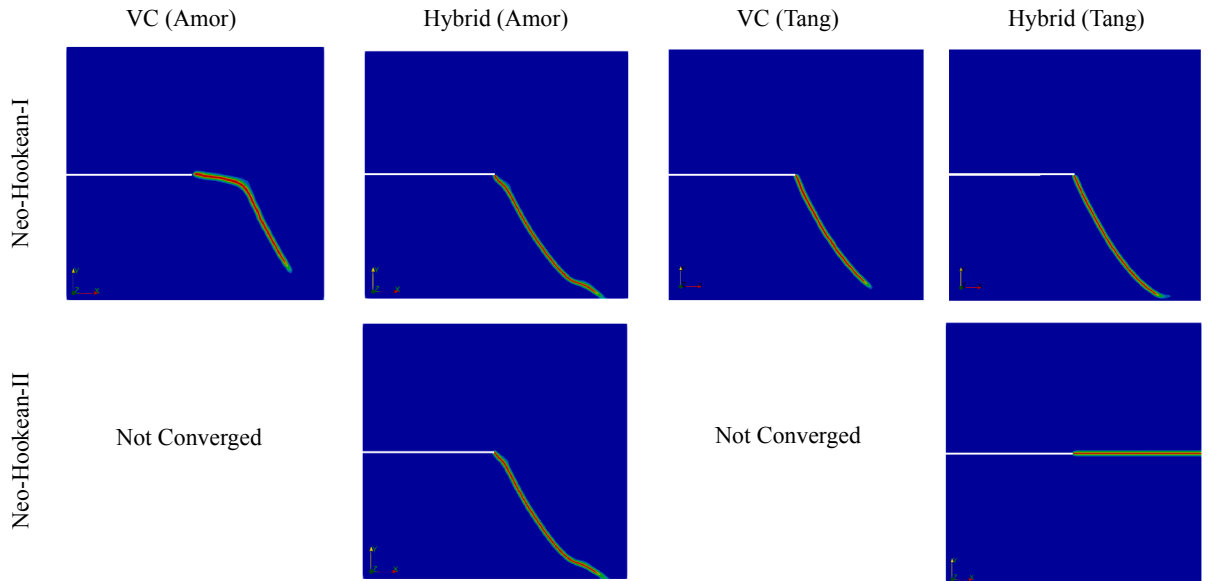


Fig. 6. Single edge notched plate in shear. effect of split on crack pattern – variationally consistent (VC) and hybrid formulation using Tang et al. and Amor et al.'s split for Neo-Hookean-I (Top) and Neo-Hookean-II (Bottom).

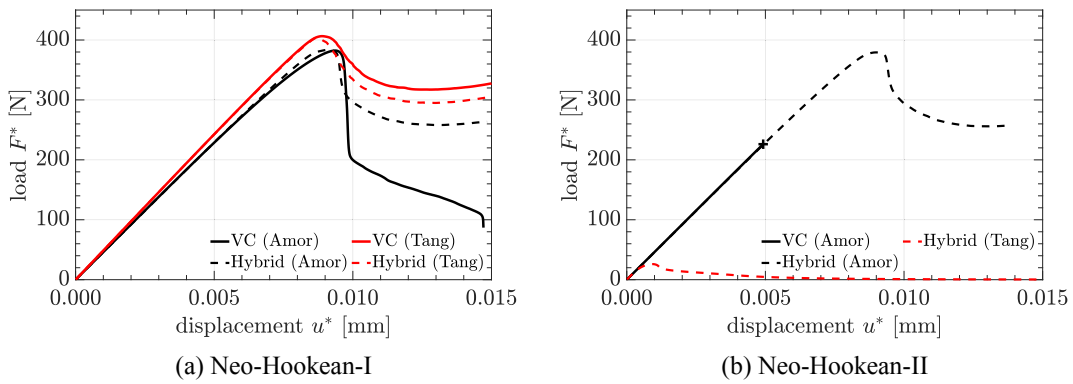


Fig. 7. Single edge notched plate in shear. effect of split on load-deformation response– variationally consistent (VC) and hybrid formulation using Tang et al. and Amor et al.'s split for Neo-Hookean-I/II.

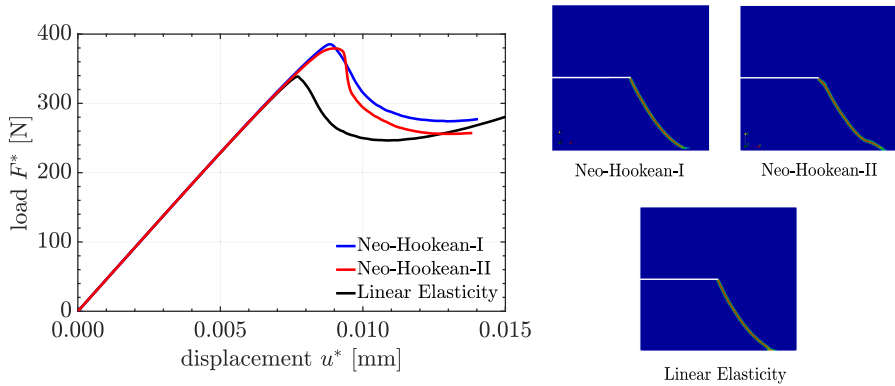


Fig. 8. Single edge notched plate in shear. Crack pattern (top) and load-deformation response (bottom). A hybrid formulation is used with Rankine type crack driving force for linear elasticity, Tang et al.’s split for Neo-Hookean-I and Amor et al.’s split for Neo-Hookean-II.

6.3. Penny shaped pre-cracked specimen

A rectangular specimen with a penny shaped initial notch is loaded quasi-statically via an imposed displacement on the top edge while the bottom one restrained vertically (Fig. 10a). This specimen is modeled using Neo-Hookean-II (as it provides a smoother softening and better for convergence in the crack propagation regime) without strain energy split. The material parameters are taken from Miehe and Schänzel [64] and provided in Table 9. Since there is no corresponding experiment, we have used an equivalent tensile strength $f_{te} = 20$ MPa calculated using Eq. (4.13) with a length scale of $b_{AT_2} = 0.0085$ mm, which is close to the length scale used by Miehe and Schänzel. However, the linear elastic formulation for the AT2: $b = \left(\frac{27}{256}\right)\left(\frac{E_0 G_f}{f_{te}^2}\right)$ also provides a quite similar estimation. Four-noded linear elements are used with effective element size $h \leq b/5$ in the region of expected crack path i.e., the mid-plane of the specimen that contains the notch.

To capture the steep load drop, from (d) to (e) in Fig. 10b, tiny displacement increments must be used. Particularly, we have used a displacement increment $\Delta u^* = 1 \times 10^{-3}$ mm up to the peak load and $\Delta u^* = 1 \times 10^{-6}$ mm thereafter. For these minuscule steps, single-iteration AM solver is sufficient. And that was the solver we used for this problem. And note that no viscous regularization nor residual strength i.e., $\kappa = 0.0$ was used. An adaptive displacement increment [80,73,51,31] might be used as a cost-effective alternative.

The load-deformation response and fracture process are shown in Fig. 10b and 11, respectively. First, the rectangular specimen got stretched in height and compressed in length until it reaches its load carrying capacity; cf. Fig. 11(a,b). Then crack initiates at the notch-edges due to concentration of tensile stress and propagates horizontally; which causes increase in length while keeping the height of specimen almost constant.

Next, we study the sensitivity of the numerical solutions with respect to the length scale b and mesh convergence. The PF-CZM results are mesh objective (Fig. 12a) and almost insensitive to length scale parameter (Fig. 12b). This attribute of the PF-CZM is due to the fact that the damage threshold and peak stress are independent of the length scale as observed from the 1D analytical homogeneous solution in Section 4. However, the AT1/2 result are sensitive to the length scale parameter as shown in Fig. 13a and b, respectively. Miehe and Schänzel [64] reported the same finding for the AT2.

With all superior attributes of the PF-CZM compared with the AT1/2, one might ask whether it is more computationally demanding. To answer this question, we have tested the efficiency of these three models for same length scale $b = 0.01$ mm with mesh

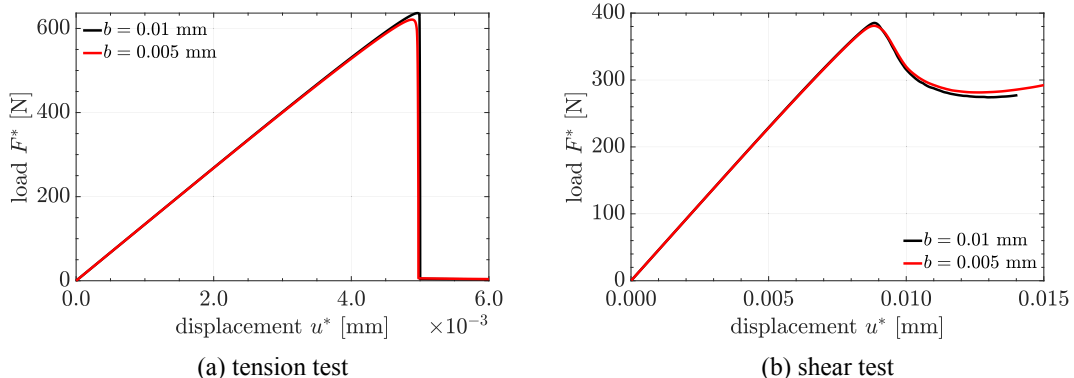


Fig. 9. Single edge notched plate: the PF-CZM provide length scale insensitive results (Neo-Hookean-I).

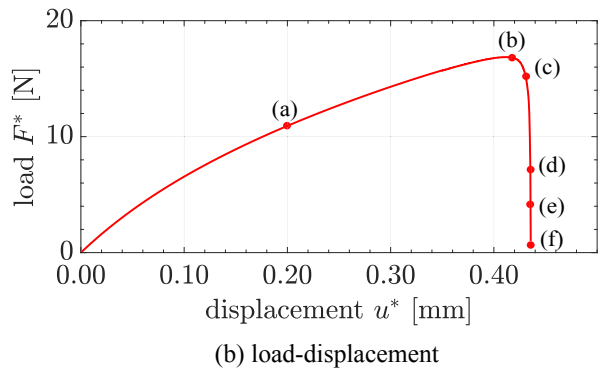
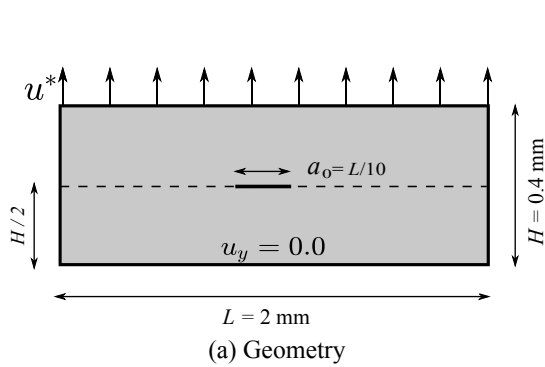


Fig. 10. Penny shaped pre-cracked specimen: schematic geometry and loading (a) and load-displacement response (b). The bottom edge is fixed in the vertical direction. Thickness of specimen = 1 mm and notch width = 0.005 mm. The load-displacement curves are supplemented with markers to show the corresponding fracture stage in Fig. 11.

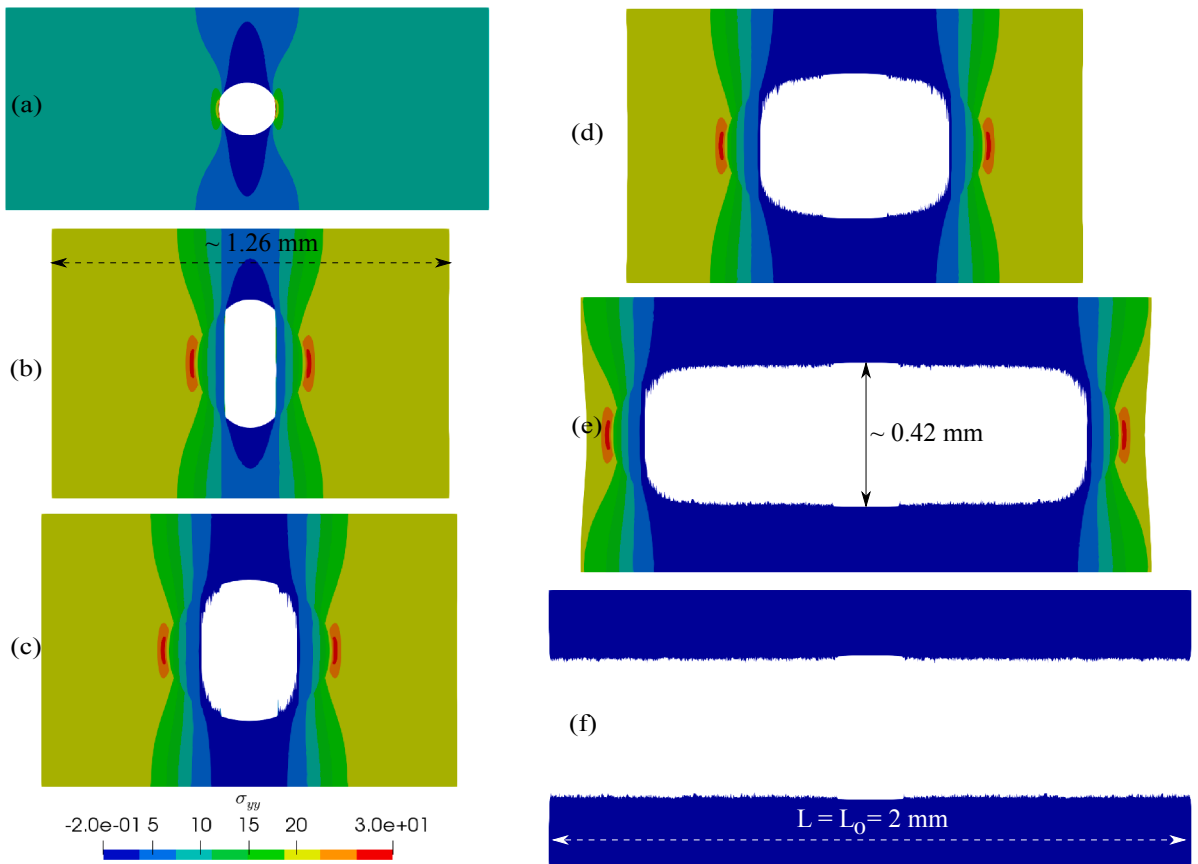
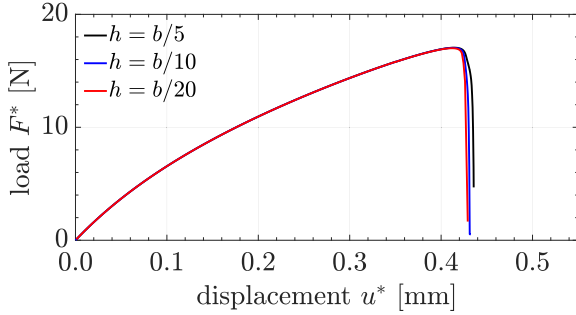
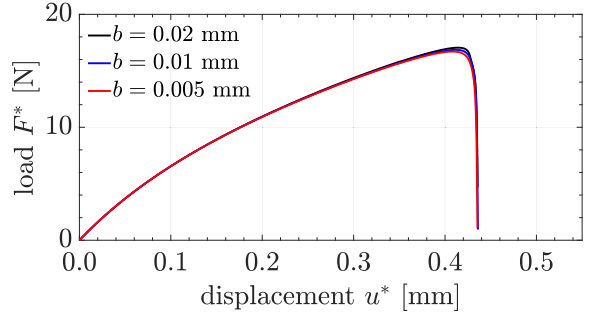
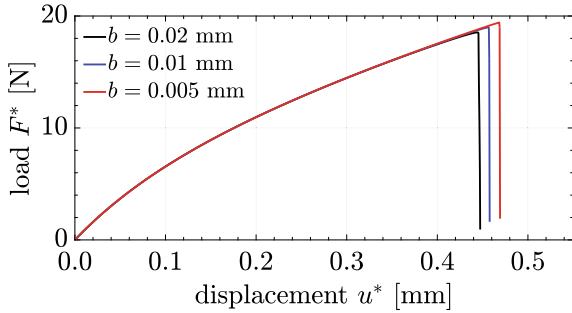
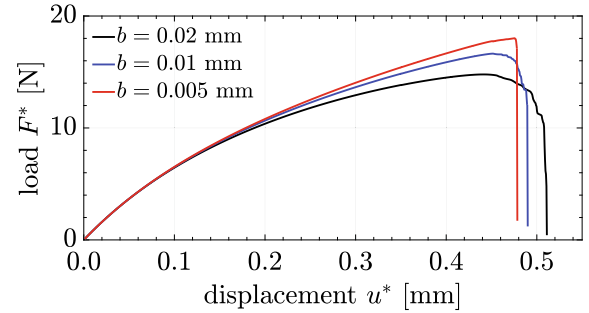


Fig. 11. Penny shaped pre-cracked specimen: deformed shape (without magnification, and this applies to all deformed configuration plots hereafter) at different instances of loading as marked on the load-displacement response in Fig. 10b: (a) $u^* = 0.2 \text{ mm}$, (b) $u^* = 0.42 \text{ mm}$, (c) $u^* = 0.43 \text{ mm}$, (d) $u^* = 0.4339 \text{ mm}$, (e) $u^* = 0.43545 \text{ mm}$, (f) $u^* = 0.43565 \text{ mm}$. Elements with damage $d \geq 0.8$ are removed to show the crack. However, a larger damage threshold e.g. $d \geq 0.95$ does not change the crack path mainly due to finiteness of damage band width of PF-CZM – this is valid for all figures in this paper. The color is the Cauchy stress σ_{yy} .

$h = b/5$. Despite having a complex rational degradation function, PF-CZM needs less number of Newton-Raphson iterations to converge than AT2 due to the presence of an elastic domain and comparatively smoother behaviour in the softening regime; cf. Fig. 14a. On the other hand, the PF-CZM and AT1 take almost similar computation time for this test. The AT1 demands less Newton-Raphson iterations for the damage sub-problem, but the displacement sub-problem is more expensive (cf. Fig. 14b) due to steep load drop after peak load (Fig. 14c). This observation is similar to linear elastic PFM as observed in [58] and outlined in Table 1.

(a) mesh convergence ($b = 0.02 \text{ mm}$)(b) length scale convergence ($h = b/5$)**Fig. 12.** Penny shaped pre-cracked specimen: sensitivity of load-deformation response to length scale b and element size h for PF-CZM.

(a) AT1



(b) AT2

Fig. 13. Penny shaped pre-cracked specimen: length scale sensitive load-deformation response of AT1/2 for $h = b/5$.

Remark 6.1. The AT2 model usually enjoys a more efficient implementation by Miehe et al. [66] where the condition $\dot{d} \geq 0$ is dealt with by a history variable (representing the maximum ψ_0^+). In that implementation, the damage sub-problem is simply a linear problem [66] where the damage boundedness $0 \leq d \leq 1$ is automatically satisfied. Loew et al. [51] demonstrated that Miehe's implementation yields erroneous results for the rate-dependent formulation: damage continues to grow when the strain decreases. We prefer the unified implementation, presented in Section 5, which can deals with any phase field model and handles $\dot{d} \geq 0$ correctly. \square

6.4. Symmetric double edge notched specimen

Hocine et al. [38] carried out experiments on symmetric double edge notched specimens made of styrene butadiene rubber for different initial notch sizes (Fig. 16a). Recently, Miehe and Schänzel [64] and Tang et al. [82] simulated this experiment using the AT2 model. Herein, we reconsider it using the proposed finite deformation PF-CZM. Since it is a mode-I fracture problem, the Neo-Hookean-II material without strain energy split is considered which is better for convergence in the softening regime.

As Hocine et al. [38] did not report the material tensile strength or the failure strain, we have calibrated f_{te} in Section 6.4.1. Then, our simulation results are presented in Section 6.4.2.

6.4.1. Estimation of material parameters

First, we have verified the elasticity parameters, Young's modulus $E_0 = 0.5887 \text{ MPa}$ and Poisson's ratio $\nu_0 = 0.45$ as used by Miehe and Schänzel, by carrying out a uniaxial tension test (Fig. 15a). Arbitrarily large values for G_f and f_{te} were used to avoid damage in the specimen.

Next, the equivalent tensile strength f_{te} is estimated from mode-I fracture simulation of the specimen of notch size $a_0 = 28 \text{ mm}$ with given $G_f = 2.67 \text{ N/mm}$ [64] and the verified elasticity parameters. A best fit value $f_{te} = 0.65 \text{ MPa}$ is obtained (Fig. 15b). The material parameters are given in Table 9. Moreover, the material tensile strength is estimated as $f_t = 0.58 \text{ MPa}$ using Eq. (4.11) for future reference.

6.4.2. Simulation results

Using the verified and calibrated material parameters we have simulated the mode-I fracture of the double edge notched specimen for different initial notch size $a_0 = \{12, 16, 20, 24, 28\} \text{ mm}$. Four-noded linear elements are used with effective element size $h \leq b/5$, with $b = 1.0 \text{ mm}$, in the fractured region i.e., close to the plane that contains the notches. Numerical load-deformation responses are quite matching with experimental observations (Fig. 16b).

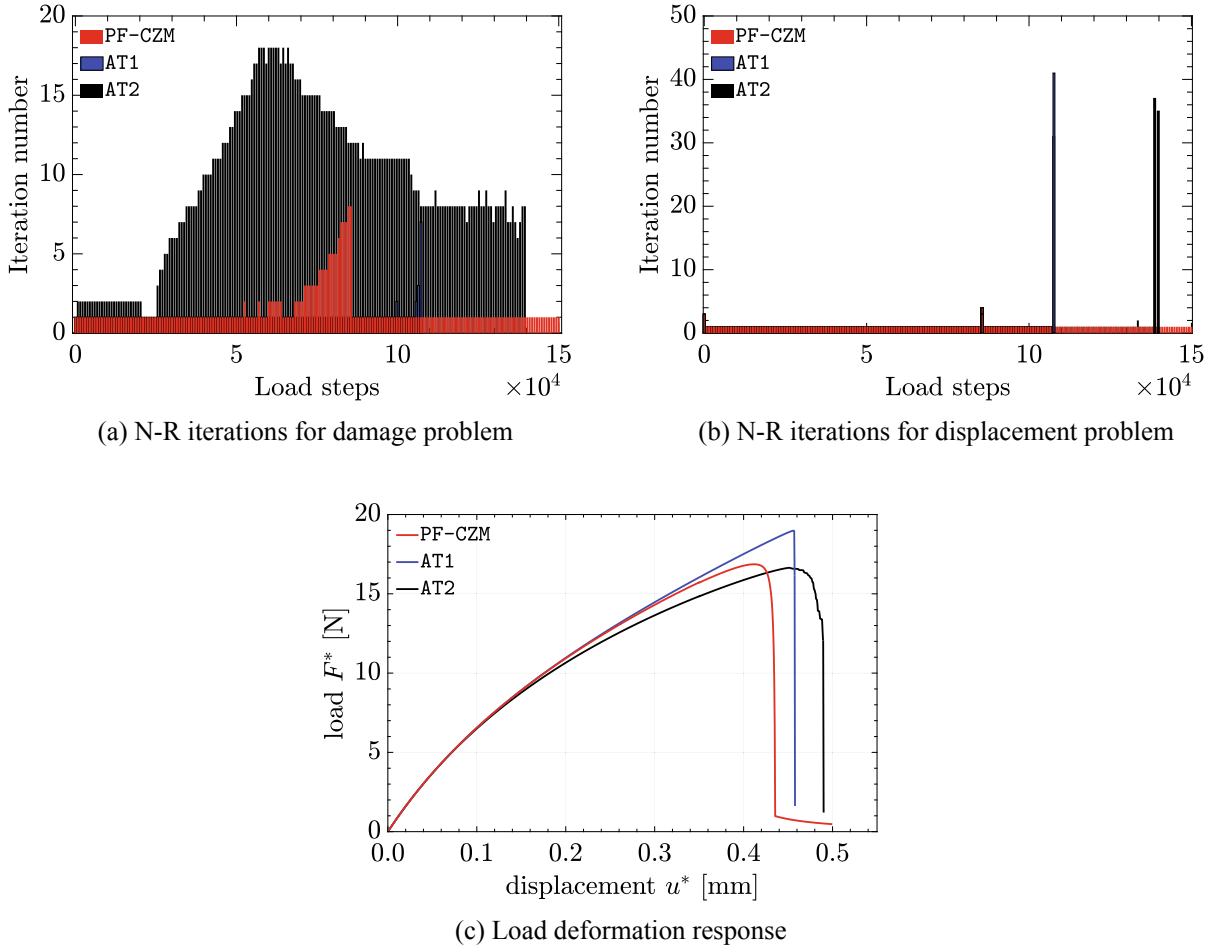


Fig. 14. Penny shaped pre-cracked specimen: efficiency of PFMs. Tested for $b = 0.01$ mm with $h = b/5$.

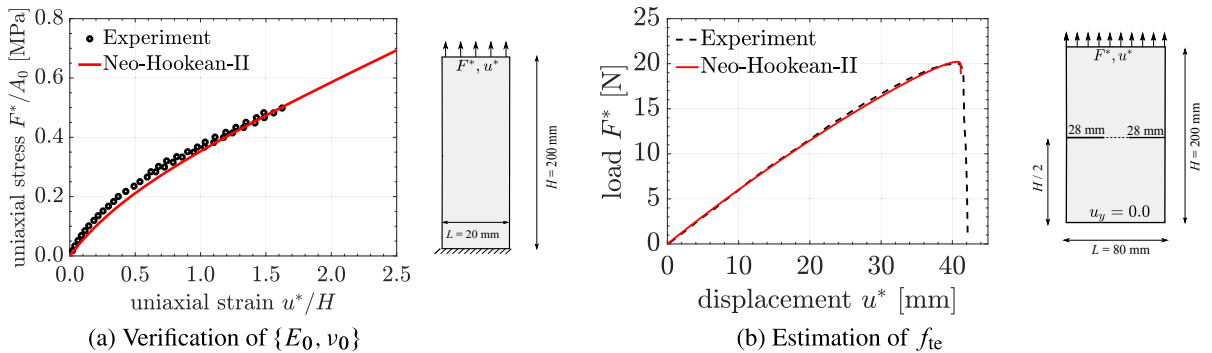


Fig. 15. Symmetric double edge notched specimen: estimation of material parameters from experimental observations – (a) estimation of elasticity parameters from uniaxial response; A_0 represents the initial cross-sectional area of the specimen. (b) estimation of fracture parameters from a mode-I fracture. Thickness of the specimen = 3.0 mm.

Hyperelastic phase field fracture is prone to numerical divergence problems in the crack propagation regime. We have resolved this issue in the previous example using the single step AM solver with minuscule displacement increments (see Section 6.3). Doing so is not cost-effective, so we tried the implicit-explicit solver. Using this solver, first a displacement increment $\Delta u^* = 0.001$ mm is used for quasi-static steps (in Fig. 16b solid lines represent the quasi-static solution). A damage threshold about 0.9 is considered as a switch to the explicit solver in which a time step $\Delta t = 0.1 \mu\text{s}$ is used keeping the displacement fixed ('chain-dotted' lines designate the explicit dynamics solution in Fig. 16b). Furthermore, a local damping with a small damping factor $\zeta = 0.01$ is adopted to reduce oscillations [43]. The results shown in Fig. 16b are obtained with this implicit-explicit solver.

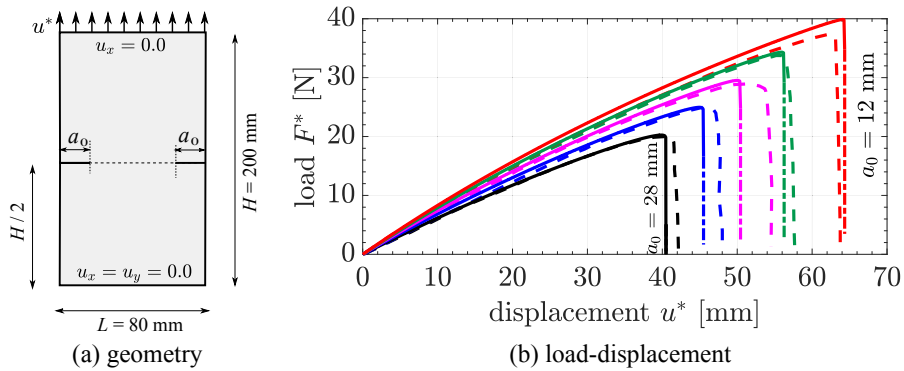


Fig. 16. Symmetric double edge notched specimen: (a) schematic geometry and loading for three different initial notch size $a_0 = \{12, 16, 20, 24, 28\}$ mm. Thickness of specimen = 3 mm and a thin notch of width = 0.5 mm is considered for simulation; (b) load-deformation response, experimental observations shown using dashed lines of same color. (For interpretation of the references to color in this figure legend, the reader is referred to the web version of this article.)

The AM solver with a viscous regularization of damage proposed by Miehe et al. [66], as presented in Section 5.2.2, is quite popular. And its implementation is easier than the implicit-explicit solver. Therefore, we tested its performance by considering different values of viscosity parameter $\frac{\xi b}{G_f} = : \xi = \{0.0, 0.04, 0.4\}$. Constant displacement increments of $\Delta u^* = 0.001$ mm are used. No viscous regularization ($\xi = 0.0$) resulted in divergence in the displacement sub-problem and thus the simulation of the complete fracture was not achieved. And this issue is resolved with larger ξ ; however, the failure load and the failure displacement are increased (Fig. 17a). The solution corresponds to $\xi \rightarrow 0$ coincides with the solution using implicit-explicit solver. Moreover, implicit-explicit solver is almost two times faster than the implicit solver with viscous regularization.

Length scale sensitivity of load-deformation response has been studied with $b = \{1.00, 0.50\}$ mm with element size $h = b/7$ in the region of expected crack path for $a_0 = 28$ mm. The PF-CZM provides a length scale insensitive response for this problem (Fig. 17b).

Fig. 18 presents the crack evolution in the deformed specimen for $a_0 = 12$ mm. The first four figures correspond to quasi-static step with (a) $u^* = 0.00$, (b) $u^* = 40.00$ mm, (c) $u^* = 60.00$ mm, (d) $u^* = 64.35$ mm; followed by explicit dynamics solution at $u^* = 64.35$ mm for different time (e) $t = 2.00$ ms, (f) $t = 8.3$ ms and (g) $t = 9.0$ ms.

6.5. Mixed mode fracture

Pidaparti et al. [75] has carried out an extensive set of experiments to study mixed-mode fracture of rubber where thin rectangular specimens with initial inclined notches are stretched vertically while keeping the bottom edge restrained vertically. They have reported critical load for crack initiation and final failure for different specimens shown in Fig. 19. Heydari-Meybodi et al. [35] have validated these results using an effective stretch criterion.

In this study, Neo-Hookean-I with volumetric-stretching type decomposition [82] is considered, because this combination is found most suitable for mixed mode fracture as discussed in Section 6.2. A plane stress state is assumed for 2D simulation; see Appendix B for numerical implementation of plane-stress hyperelasticity. As we are the first to simulate these experiments using a PFM, we need first to calibrate material parameters (Section 6.5.1). The issues related to numerical convergence for this problem is discussed in Section 6.5.2 and our simulation results are presented in Section 6.5.3.

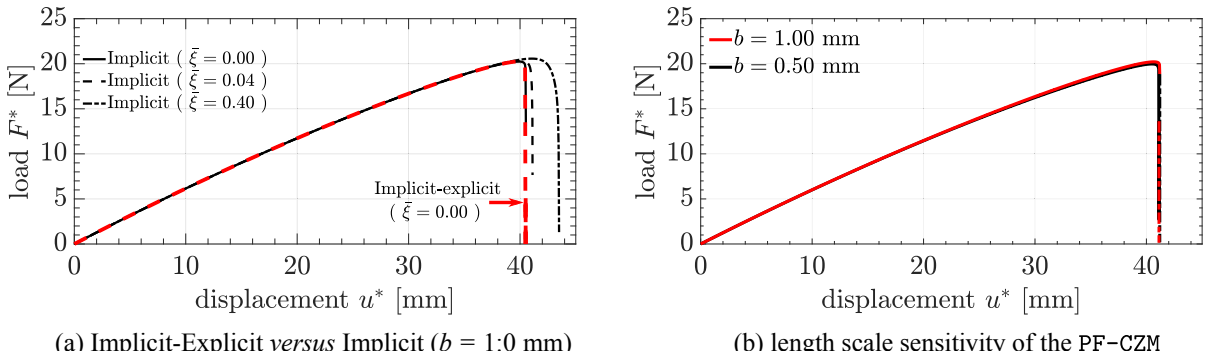


Fig. 17. Symmetric double edge notched specimen: (a) implicit solver converges to an implicit-explicit solution for viscosity parameter $\xi \rightarrow 0$; (b) length scale sensitivity study using implicit-explicit solution. Results corresponds to $a_0 = 28$ mm.

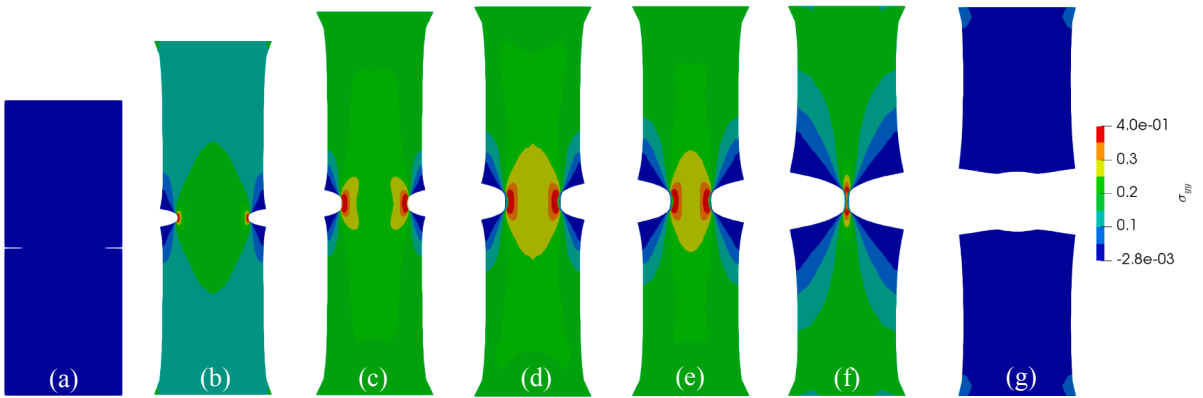


Fig. 18. Symmetric double edge notched specimen: deformed shape at different instances. Elements with damage $d \geq 0.8$ are removed to show the crack. Evolution is shown on contour of Cauchy stress σ_{yy} for $a_0 = 12$ mm.

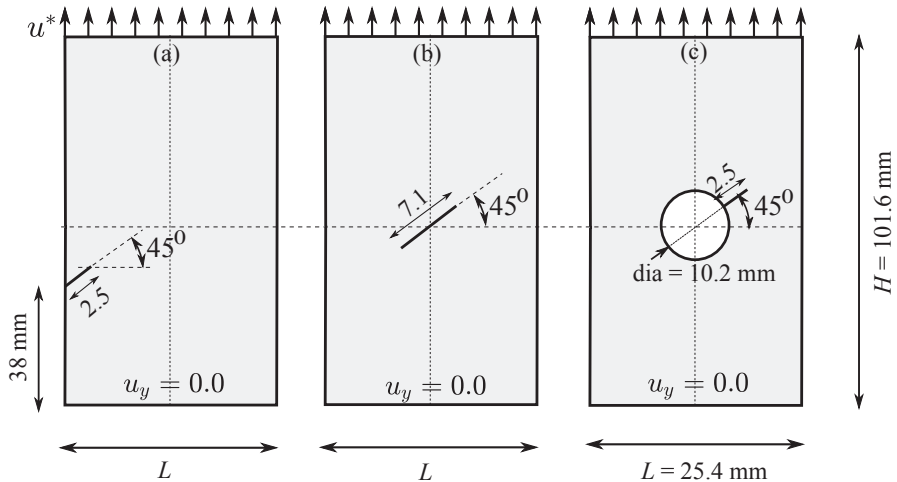


Fig. 19. Mixed mode fracture: schematic geometry and loading for three different location and geometry of notches: (a) edge notch, (b) center notch, (c) circular hole with notch. Width of notches = 0.2 mm and thickness of specimen = 2.1 mm.

6.5.1. Estimation of material parameters

The material parameters of Neo-Hookean-I have been estimated from the uniaxial test and a mode-I tearing test results carried out as part of the experiment [75]. First, the Young modulus E_0 is estimated by carrying out a uniaxial tension test similar to Section 6.1 along with the geometric dimensions as shown in Fig. 20a. Large values for G_f and f_{te} were used to avoid any damage in simulation. A best fit $E_0 = 6.5$ MPa is found to equivalently represent the experimental uniaxial response (initial regime). It is also quite obvious from the plot that one need to use a more complex material model e.g. Arruda-Boyce type Neo-Hookean model [8,35] for better fit – which is beyond the scope of the current study. Poisson's ratio $\nu_0 = 0.45$ is assumed similar to other numerical examples.

Next, the material fracture energy G_f and equivalent tensile strength f_{te} is estimated from the mode-I tearing test. Pidaparti et al. [75] has reported $G_f = 12.5 - 24.5$ N/mm with corresponding failure load $F_f^* = \{105 - 142\}$ N. We have considered $G_f = 15$ N/mm and simulated this mode-I fracture using the PF-CZM for different chosen values of f_{te} . A value of 20 MPa provides a reasonably matched failure load as shown in Fig. 20b and used for further simulation of mixed mode fracture. The material parameters are summarised in Table 9. Moreover, the material tensile strength is estimated as $f_t = 14.95$ MPa using Eq. (4.13) for future reference.

6.5.2. Numerical robustness

As we have discussed earlier, numerical robustness is a big issue for hyperelastic phase field fracture simulations and this is even worse for this large deformation plane stress fracture problem. To demonstrate the issue, we used two solvers: an implicit solver and an implicit-explicit solver.

First, an implicit solver was tried using a displacement increment up to $\sim 1 \times 10^{-6}$ mm with zero residual strength and artificial viscosity i.e., $\kappa = 0.0$, $\xi = 0.0$. We observed divergence of the Newton-Raphson solver in the displacement sub-problem at the very beginning of crack propagation. This issue in convergence was due to the local buckling instability of damaged elements, which resulted in an oscillatory and unstable motion of the compressive strain components about the equilibrium solution, and no

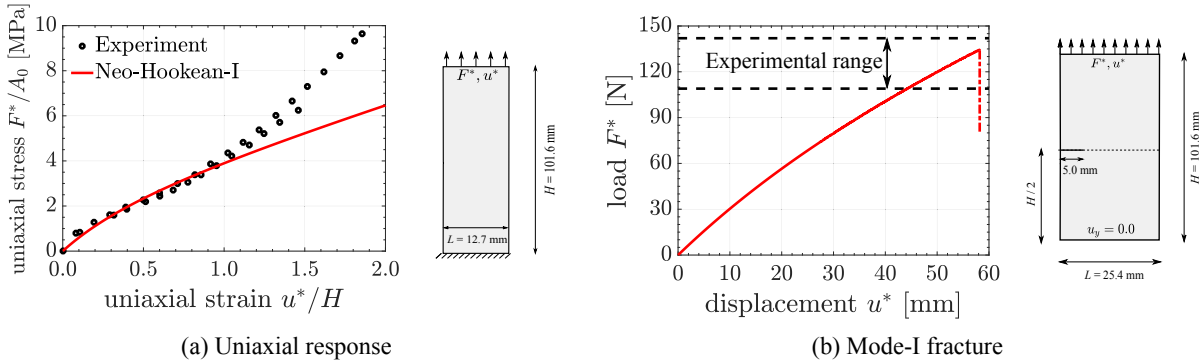


Fig. 20. Mixed mode fracture: estimation of material parameters from experimental observations – (a) Estimation of elasticity parameters from uniaxial response; A_0 represents the initial cross-sectional area of the specimen. (b) Estimation of fracture parameters from mode-I fracture. Thickness of the specimen = 2.1 mm.

significant improvement in L_2 norm was observed by reducing the displacement increments any further using multiple alternatives of conventional iterative solvers and pre-conditioners. Then a nonzero residual $\kappa \leq 0.1$ along with viscosity parameter $\frac{\eta}{G_f} = : \xi \leq 1.333$ was tried with $\Delta u^* = 0.001$ mm. The implicit solver converges for large value residual; see Fig. 21(a). A large residual strength slows down the crack propagation with a reduced crack driving force $(1 - \kappa)\omega_0'(d)\psi^+$ until $d = 1.0$ and results in larger peak load. Moreover, it also modifies the re-distribution of stresses and provides a nonzero crack driving force near the damaged region; which results in damage widening as shown in Fig. 21Right).

Finally, we have resolved this issue using a implicit-explicit solver with $\kappa = 0.01$ and $\xi = 0.133$ which enables us to simulate the

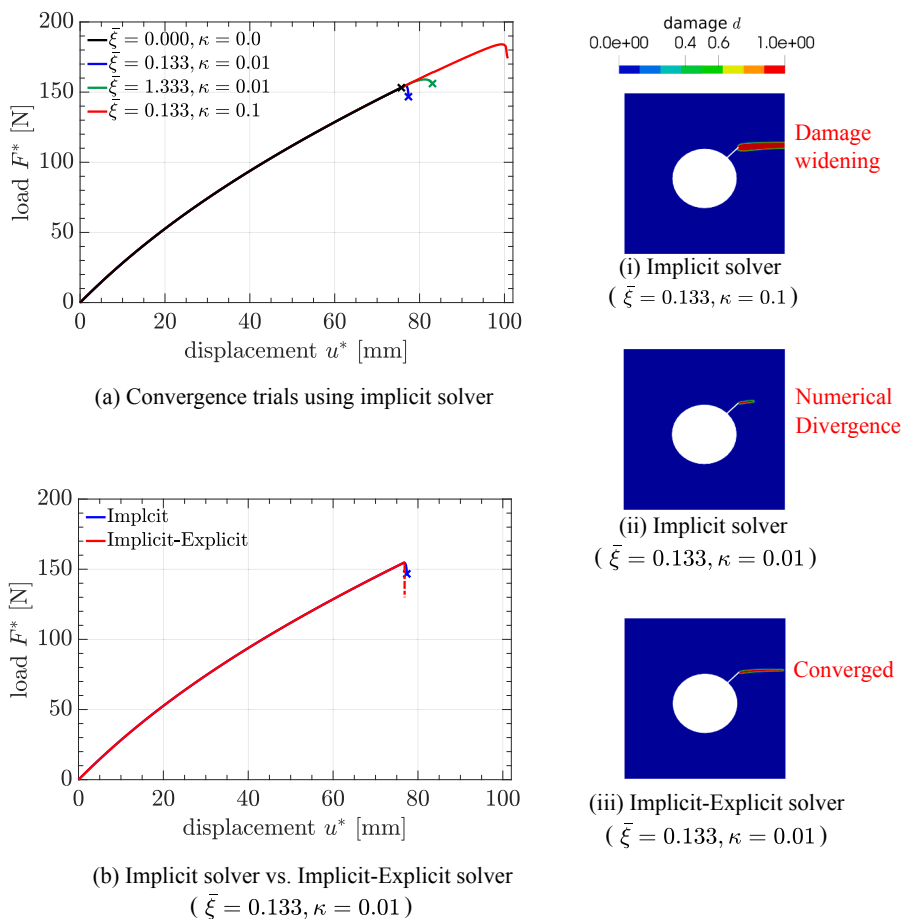


Fig. 21. Mixed mode fracture: numerical convergence study. Results are provided for the problem with circular hole, $b = 0.2$ mm and $h = b/5$. The 'X' marks on load-deformation plots represents numerical divergence of solver before complete crack propagation up to the right edge.

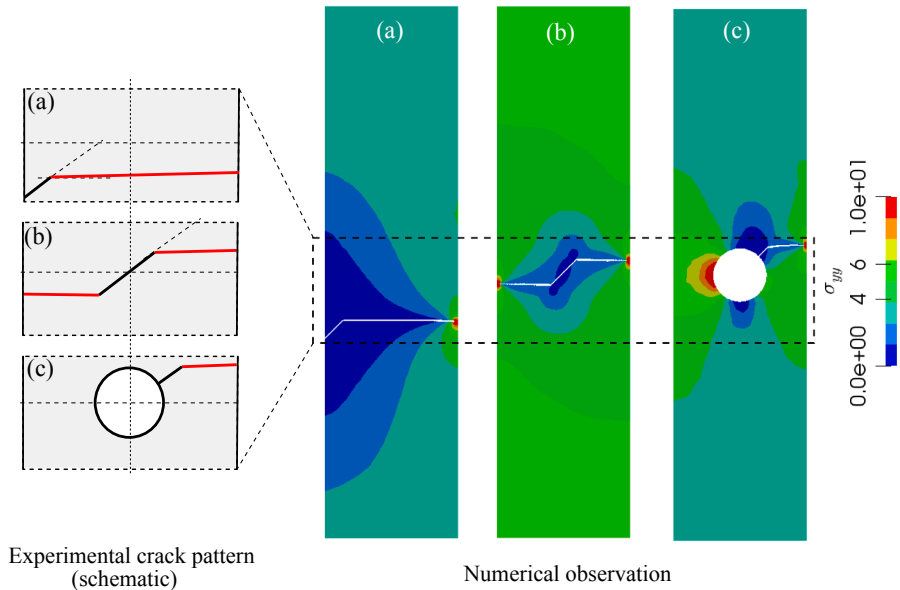


Fig. 22. Mixed mode fracture: schematic representation of experimental crack pattern from Pidaparti et al. [75] (left). Numerical crack pattern is shown on contour of Cauchy stress σ_{yy} (right). Elements with damage $d \geq 0.8$ are removed to show the crack.

entire crack propagation without damage widening. This also provides the global load-deformation response very close to the case with zero viscosity and zero residual. A displacement increment $\Delta u^* = 0.001$ mm is used for quasi-static steps followed by explicit solver with a time step $\Delta t = 0.1 \mu\text{s}$ and a small velocity $v_0 = 0.01$ mm/s at the top edge. A damage threshold about 0.9 is considered as a switch to the explicit solver. Furthermore, a local damping with a small damping factor $\zeta = 0.01$ is adopted to reduce oscillations [43].

6.5.3. Simulation results

The final numerical crack patterns shown in Fig. 22 are in good agreement with the experimental observations: starting from the notch tip, a crack is initiated and grows nearly horizontally until it reaches the sample's vertical edge. We present the crack propagation in Fig. 23 for different notch locations. For each case, the first two figures corresponds to quasi-static step with (a)

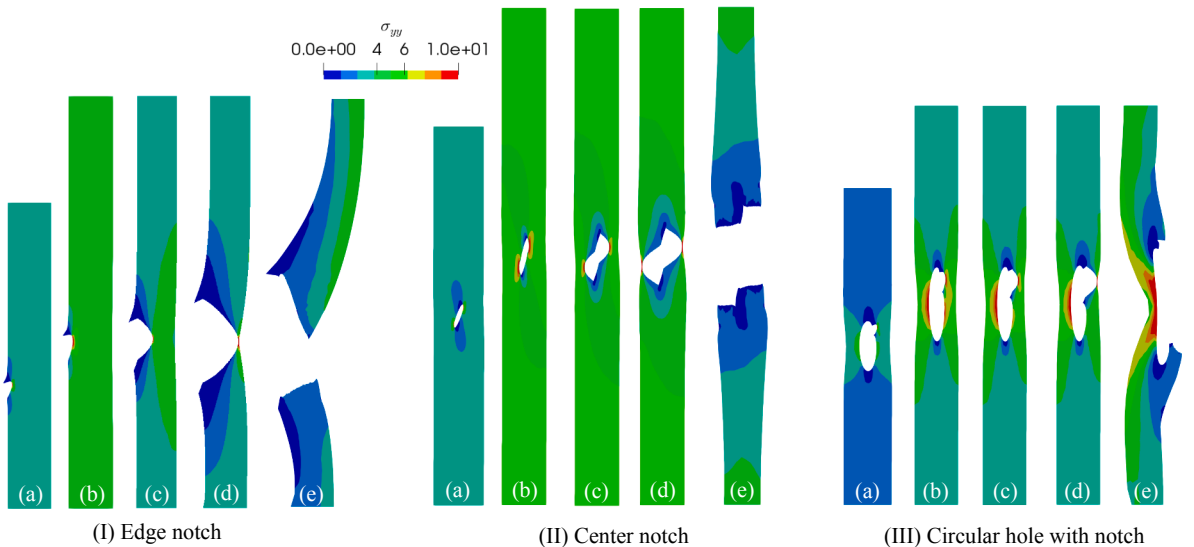


Fig. 23. Mixed mode fracture: deformed shape at different instances. Results for different notch types – Edge notch (Left), Center notch (Middle), Circular hole with notch (Right). Elements with damage $d \geq 0.8$ are removed to show the crack. Evolution is shown on contour of Cauchy stress σ_{yy} .

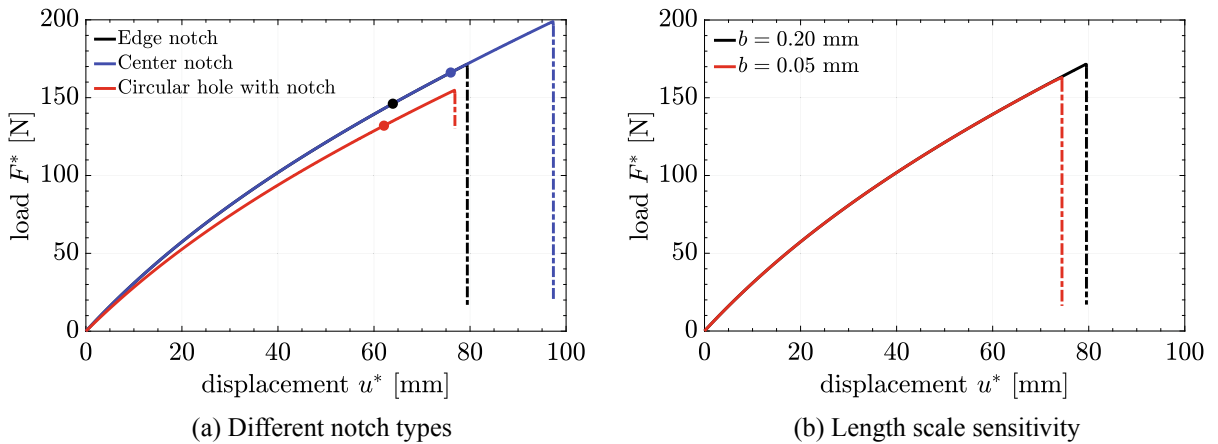


Fig. 24. Mixed mode fracture: (a) load-deformation response for different notch types. Crack initiation corresponds to $\frac{\Psi_e}{\Psi_s} \approx 1 \times 10^{-5}$ as marked on each plot. (b) length scale sensitivity for the edge notched specimen.

$u^* = 0.5u_{\max}$, (b) $u^* = u_{\max}$; followed by explicit dynamics solution at $u^* \sim u_{\max}$ for different time instances (c) $t = 0.5t_{\max}$, (d) $t = 0.95t_{\max}$, (e) $t = t_{\max}$. The maximum applied displacement $u_{\max} = \{79.44 \text{ mm}, 97.36 \text{ mm}, 76.85 \text{ mm}\}$ and failure time $t_{\max} = \{0.67 \text{ s}, 0.29 \text{ s}, 0.20 \text{ s}\}$ for three notch types, respectively.

The numerical load-deformation response is shown in Fig. 24a where solid lines representing the implicit quasi-static solution are followed by 'chain-dotted' lines showing the explicit dynamics solution. Load-deformation response are almost identical for the edge notched and centrally notched specimen until the softening. Contrary to the other specimens, the load capacity of the specimen with a circular hole is nonzero at the end of the simulation as the crack does not separate the specimen into two pieces.

Next, the length scale sensitivity of the load-deformation response is studied for the edge notched specimen with $b = \{0.20 \text{ mm}, 0.05 \text{ mm}\}$ and $h = b/5$. The load deformation response is considerably less sensitive to the length scale parameter as shown in Fig. 24b – difference in peak loads $\sim 5\%$. Understanding this (small) length scale sensitivity of PF-CZM, which have provided b -insensitive responses for other examples, is not very clear so far – there might be multiple geometric and model parameters responsible for this – it is a ongoing research.

We now present a quantitative comparison of the numerical and experimental failure loads. It is tricky to estimate the load corresponding to crack initiation – for brittle problems with notches, we might observe a non-zero damage at the beginning of loading and this varies based on the notch geometry. This first non-zero damage are not usually observable during the laboratory experiment. For post-processing, we have defined crack initiation when the ratio of surface energy to stored energy $\frac{\Psi_e}{\Psi_s}$ exceeds 1×10^{-5} . Numerical estimation of failure loads for different geometry are within the range of experimental observations, cf. Table 10.

7. Conclusions

This paper has presented a length-scale insensitive phase field model for hyperelastic brittle fracture (PF-CZM). The major findings of this work includes:

- Similar to the AT1/2, the PF-CZM is equally applicable for fracture of rubber-like elastomers.
- In contrast to other PFM's which are length scale sensitive, the PF-CZM provides length scale insensitive response for hyperelastic fracture.

Table 10

Mixed mode fracture: applied load at crack initiation and final failure (unit N).

Specimen	Crack initiation		Final failure	
	PF-CZM	Experiment	PF-CZM	Experiment
(a) Edge notch	146	160–189	171	191–254
(b) Center notch	165	116–138	198	180–234
(c) Circular hole with notch	130	102–151	154	120–169

Table 11

Summary of the simulation time in hours. The number of cores used for a particular simulation is shown in parentheses. First two rows are using implicit solver whereas bottom two are using implicit-explicit solver. The shear test is considered here for Section 6.2. The centrally notched specimen is considered from Section 6.5.

Example	Dimensions [mm]	Elements	Nodes	b [mm]	Δu	u_{\max} [mm]	Sim. time [Hrs]
Section 6.2	1.0×1.0	2.5×10^5	1.2×10^5	0.01	1×10^{-5}	0.02	50 (8)
Section 6.3	2.0×0.4	1.6×10^4	1.7×10^4	0.01	1×10^{-6}	0.435	11 (16)
Section 6.4	80×200	2.0×10^4	1.2×10^4	1.0	1×10^{-3}	43.2	9.5 (8)
Section 6.5	25.4×101.6	7.0×10^4	3.6×10^4	0.2	1×10^{-3}	97.4	80 (8)

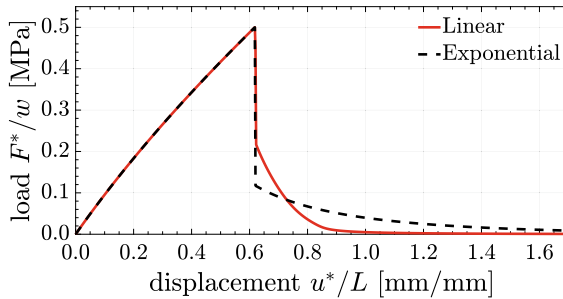


Fig. 25. An uniaxial bar: load-deformation response using PF-CZM for $G_f = 35$ N/mm and $\sigma_{\max} = 0.5$ MPa.

- Despite having a complex rational degradation function, PF-CZM is less expensive than AT2 for hyperelastic fracture as well due to presence of elastic domain and a smoother softening regime; when tested using a unified implementation applicable for any PFM as demonstrated in this study.
- The standard compressible Neo-Hookean model [95] and the simplified version proposed by Miehe and Schäanel [64] are equally good for mode-I hyperelastic fracture. However, the standard Neo-Hookean model with a principal stretch based decomposition [82] is seemed to be a better alternative for mixed-mode fracture problems.
- The multi-step alternating minimization (AM) solver is not robust in the softening regime due to its non-monotonic convergence. A single-step AM solver with viscous regularization or an implicit-explicit solver is recommended for hyperelastic fracture. Also there is a need for more generalized and robust solver for hyperelastic phase field fracture.
- A convergence issue of hyperelastic fracture due to the probable local buckling instability of damaged elements, is observed for the first time in phase field fracture – which is effectively resolved using an implicit-explicit solver along with viscous regularization and residual strength.
- Using large residual strength to get a smoother softening (and thus a better convergence) may result in damage widening and significantly increased load carrying capacity. Thus, a limiting value for this residual is observed to be $\kappa \sim 0.01$.

Phase field fracture models usually subject to a criticism about its computational cost. To have a better view on this, we present in Table 11 the computational cost of hyperelastic fracture simulations presented in this study. Simulations are carried out using parallel computation on a Dell Precision 7920 Ubuntu workstation⁴. The number in parentheses represents the number of CPU cores.

The numbers in Table 11 indicate that phase field simulations using the standard alternating minimization solver is computationally demanding. Recently, Wu et al. [87] demonstrated that the BFGS (Broyden-Fletcher-Goldfarb-Shanno) monolithic solver significantly improves the efficiency of phase field simulations, see also Kristensen and Martínez-Pañeda [46]. We are investigating that solver for hyperelastic fracture phase field models.

Until now we have considered a linear softening law for the PF-CZM. This is able to model brittle fracture. Cohesive fracture can be treated using the ideas from Wu [85]. For example, with $p = 2.5$, $a_2 = 0.1748$, $a_3 = 0$ (calibrated for an exponential softening law for small strain cases), we can delay the ultimate failure (Fig. 25). Further works are needed to determine the coefficients in the rational degradation function to mimic a given softening law.

Declaration of Competing Interest

The authors declare that they have no known competing financial interests or personal relationships that could have appeared to influence the work reported in this paper.

⁴ CPU: Intel(R) Xeon(R) Platinum 8170 CPU @ 2.10 GHz; RAM: 2666 MHz 252 GB DDR4. This workstation has 104 cores.

Acknowledgments

The first author (T.K. Mandal) thanks the Monash Graduate Scholarship and Monash International Tuition Scholarship for funding his PhD. The second author (Abhinav Gupta) thanks the Ministry of Human Resource Development for funding his PhD. The third author (V.P. Nguyen) thanks the funding support from the Australian Research Council via DECRA project DE160100577. The fourth author (Rajib Chowdhury) thanks the funding support from the SERB via file No. CRG/2019/004600.

Appendix A. feFrac versus FEniCS

Besides the conventional FE implementation, where we manually code the FE vectors and matrices ourselves, there also exist FE packages/libraries that automatically generate the FE vectors and matrices based on the symbolic representation of the weak form of the problem under consideration. **FEniCS** is one such library [54,1].

We have implemented the three PFM, i.e., AT1/2 and PF-CZM using the conventional FE implementation in our in-house code **feFrac** (Section 5) and **FEniCS**. The latter allows us to focus on the physics of the problem and not the FE implementation: one does not need to manually derive the consistent material tangent for complex material models (which is a time consuming task for hyperelastic materials with a positive/negative split). However, we find that it is sometimes difficult to add functionalities to **FEniCS**, particularly when we are not so familiar with its technologies. We thus aim for a balance of using both implementations.

We present an overview of our **FEniCS** implementation in Appendix A.1 which is based on the work of Farrell and Maurini [22]. Although our primary objective of this paper is not to compare these two packages for PFM, we have used the same solver with the same order tolerances where applicable, which results in the same numerical outcomes, shown in Appendix A.2.

A.1. Overview of *FEniCS* implementation

The system Lagrangian as described by Eq. (2.3) is formulated using the unified form language ‘UFL’ [3] that helps us to describe finite element variational forms in a notation close to the mathematical notation. The discretization of the variational forms described by UFL is done with the help of **FEniCS** form compiler ‘FFC’ [44,71] to get an efficient low-level unified form-assembly code ‘UFC’ [2]. The compiled code is then evaluated by running solvers scripts available in **DOLFIN** [53] using the linear algebra backend **PetSc** [9].

Since the Lagrangian given in Eq. (2.3) is non-convex in both variables $\{u, d\}$, an alternate minimization solution scheme is adopted. For a quasi-static problem, the energy functional of displacement and damage sub-problem is equivalently expressed as,

$$\mathcal{E}_u := \int_{\Omega_0} \psi_s \left(C(u), d \right) dV - \int_{\Omega_0} \mathbf{b}^* \cdot \mathbf{u} dV - \int_{\partial\Omega_{0,t}} \mathbf{t}^* \cdot \mathbf{u} dA \quad (\text{A.1a})$$

$$\mathcal{E}_d := \int_{\Omega_0} \psi_s \left(C(u), d \right) dV + \int_{\Omega_0} G_f \gamma \left(d; \nabla_0 d \right) dV \quad \text{with } d \geq 0, \quad d = \begin{cases} 0, 1 \end{cases} \quad (\text{A.1b})$$

At minimum point of Lagrangian \mathcal{L} , as discussed in Section 2, Eqs. (A.1a) and (A.1b) are minimized alternately for u and d , respectively. The weak form (Eqs. (2.4) and (5.3)) and the Jacobian-Eqs. (5.5) and (5.13) –are computed automatically using the built-in function *derivative* – which symbolically computes the Gateaux derivative. The boundness and irreversibility of damage field (Eq. (5.12)) is implemented by specifying the bound constraints inside the nonlinear variational solver of **PetSc**. For more details please refer Farrell and Maurini [22], Hirshikesh et al. [36].

A.2. Comparison of results

This section presents a comparison of the two implementations. We have picked two examples for comparison using the PF-CZM:

- Fig. A.1a – mixed-mode fracture considering Neo-Hookean-I with Tang’s split (hybrid).
- Fig. A.1b – large deformation mode-I considering Neo-Hookean-II w/o split. A ‘posteriori’ error estimator based adaptive displacement increment [31] has been implemented in **FEniCS** and compared with uniform displacement increment using **feFrac**.

Both implementations provide quite similar results for both examples (Fig. A.1).

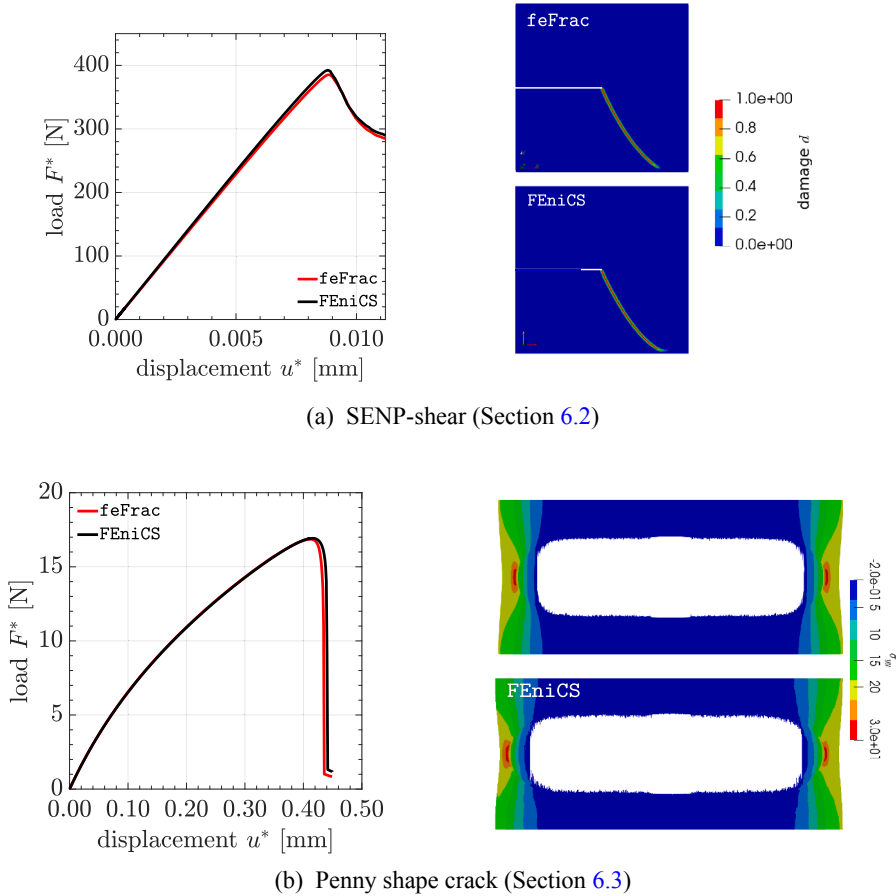


Fig. A.1. feFrac versus FEniCS: comparison of numerical results.

Appendix B. Plane stress implementation

We implement a plane stress state using a local iteration based approach of Klinkel and Govindjee [45] and also documented in Zienkiewicz et al. [95]. It is based on a linearization of the out-of-plane stress component to compute the correction in the corresponding strain component; and a static condensation of tangent modulus (matrix) for global iteration. In the procedure, we adopt the effective stress space *i.e.*, we use the undamaged stress \bar{S} and undamaged tangent modulus \bar{D} .

Denoting the out-of-plane stress by \bar{S}_{zz} and the out-of-plane strain by E_{zz} , the implementation follows the following steps:

1. Get the last converged $E_{zz}^{(i)}$. The superscript denotes the local iteration number. For global Newton-Raphson iterations, the stress state is first computed as for the plane strain condition and then, we check the plane stress condition $|\bar{S}_{zz}| < \text{tol}$. If this condition is not satisfied then the following steps are carried out to set $\bar{S}_{zz} \rightarrow 0$. Otherwise, we continue with equilibrium calculations.
2. Compute the correction for E_{zz} and update strain tensor for given value of \bar{S}_{zz} and corresponding material tangent modulus \bar{D}_{zzzz} ,

$$E_{zz}^{(i+1)} = E_{zz}^{(i)} - \bar{S}_{zz}^{(i)} / \bar{D}_{zzzz}^{(i)} \quad (\text{B.1a})$$

3. Store $E_{zz}^{(i+1)}$ as history variable. GOTO (1).
4. Upon convergence (of the local iterative process), the material tangent is condensed in order to obtain a consistent stress-strain relation. It is a standard practice to store material constitutive tangent \bar{D} using Voigt notation where normal components are stored first and then the shear components. Hence, it is necessary to bring the z - component at the last position and perform static condensation as shown in Eqs. (B.2a) and (B.2b), respectively,

$$\bar{D} = \begin{bmatrix} \bar{D}_{xxxx} & \bar{D}_{xxyy} & \bar{D}_{xxzz} & \bar{D}_{xxxy} \\ & \bar{D}_{yyyy} & \bar{D}_{yyzz} & \bar{D}_{yyxy} \\ & & \bar{D}_{zzzz} & \bar{D}_{zzxy} \\ & & & \bar{D}_{xyxy} \end{bmatrix} \Rightarrow \begin{bmatrix} \bar{D}_{xxxx} & \bar{D}_{xxyy} & \bar{D}_{xxxy} & \bar{D}_{xxzz} \\ \bar{D}_{xxyy} & \bar{D}_{yyyy} & \bar{D}_{yyxy} & \bar{D}_{yyzz} \\ \bar{D}_{xxxy} & \bar{D}_{yyxy} & \bar{D}_{xyxy} & \bar{D}_{xyzz} \\ \bar{D}_{xxzz} & \bar{D}_{yyzz} & \bar{D}_{xyzz} & \bar{D}_{zzzz} \end{bmatrix} \equiv \begin{bmatrix} \bar{D}_{mm} & \bar{D}_{mz} \\ \bar{D}_{zm} & \bar{D}_{zz} \end{bmatrix} \quad (\text{B.2a})$$

$$\bar{\mathbb{D}}_{mm} = \bar{\mathbb{D}}_{mm} - \bar{\mathbb{D}}_{mz} \bar{D}_{zz}^{-1} \bar{\mathbb{D}}_{zm} \quad (\text{B.2b})$$

5. The material tangent tensor is re-arranged to its original order.

Appendix C. Tension-compression asymmetry in hyperelasticity

The tension-compression asymmetry is modeled, in a PFM, usually by an additive split of the strain energy density. For hyperelastic fracture, there are multiple alternatives: the ‘volumetric-deviatoric’ split of Amor et al. [7], Borden et al. [14], the additive split based on principal invariants of Hesch et al. [34] and more recently, a ‘volumetric-stretch’ based decomposition of Tang et al. [82]. In this study, we consider Amor et al. and Tang et al.’s approach for their simple physical interpretations.

The starting point of almost any split is writing the undamaged strain energy density ψ_0 as summation of a deviatoric part, ψ_d , and a volumetric part, ψ_v

$$\psi_0 = \psi_d + \psi_v \quad (\text{C.1})$$

which is necessary to avoid possible mutual contradiction of parameters during split [34].

Tang et al.’s approach begins with an eigenvalue decomposition of the right Cauchy-Green deformation tensor C with eigenvalues p_n and eigenvectors β_n

$$C = \sum_{n=1}^3 p_n \beta_n \otimes \beta_n \quad \text{also,} \quad \frac{\partial p_n}{\partial C} = \beta_n \otimes \beta_n \quad (\text{C.2})$$

Physically, p_n represents the square of the principal stretches. The positive and negative part of the strain energy are written as

$$\psi_0^+ := \psi_d(p_n^+) + \psi_v(J^+) \quad \text{with } p_n^+ = \begin{cases} p_n & \text{if } p_n > 1 \\ 1 & \text{otherwise} \end{cases} \quad \text{and } J^+ = \begin{cases} J & \text{if } J > 1 \\ 1 & \text{otherwise} \end{cases} \quad (\text{C.3a})$$

$$\psi_0^- := \psi_d(p_n^-) + \psi_v(J^-) \quad \text{with } p_n^- = \begin{cases} p_n & \text{if } p_n < 1 \\ 1 & \text{otherwise} \end{cases} \quad \text{and } J^- = \begin{cases} J & \text{if } J < 1 \\ 1 & \text{otherwise} \end{cases} \quad (\text{C.3b})$$

where J is given by $J := \det F$.

For the volumetric decomposition of Amor et al. [7], one writes

$$\psi_0^+ := \psi_d + \psi_v(J^+) \quad \psi_0^- := \psi_v(J^-) \quad (\text{C.4})$$

with the same definition of J^\pm as in Eq. (C.3). Amor’s approach [7] can be seen as a special case of Tang et al.’s decomposition.

Next, we present herein some derivation steps to obtain the volumetric-stretching split of Tang et al. [82] for Neo-Hookean-I material. This does not repeat the cited work because unlike Tang et al. [82] who adopted the unsymmetric first Piola-Kirchoff stress, we employ the second Piola-Kirchoff stress in the formulation. Additionally, we present expressions for the PK2 stress and material tangent.

Following the eigenvalue decomposition of the right Cauchy-Green deformation tensor (Eq. (C.2)), we write the strain energy density ψ_0 for Neo-Hookean-I, as provided in Table 3, as a combination of $\psi_d(p_n, \beta_n)$ and $\psi_v(J)$

$$\psi_0 = \underbrace{\frac{\mu_0}{2}(\text{tr}(C) - 3 - 2\log J)}_{\text{deviatoric, } \psi_d} + \underbrace{\frac{\lambda_0}{2}(\log J)^2}_{\text{volumetric, } \psi_v} = \frac{\mu_0}{2} \sum_{n=1}^3 \underbrace{(p_n - 1 - \log p_n)}_{\bar{\psi}_{d,n}} + \frac{\lambda_0}{2} \underbrace{(\log J)^2}_{\bar{\psi}_v} \quad (\text{C.5a})$$

$$\psi_0^+ = \frac{\mu_0}{2} \sum_n \bar{\psi}_{d,n} |_{p_n > 1} + \frac{\lambda_0}{2} \bar{\psi}_v |_{J > 1}, \quad \psi_0^- = \frac{\mu_0}{2} \sum_n \bar{\psi}_{d,n} |_{p_n < 1} + \frac{\lambda_0}{2} \bar{\psi}_v |_{J < 1} \quad (\text{C.5b})$$

The effective stress \bar{S}_{ij} and its positive/negative parts can be written as

$$\bar{S}_{ij} = \mu_0(\delta_{ij} - C_{ij}^{-1}) + \lambda_0 \log J C_{ij}^{-1} = \mu_0 \sum_{n=1}^3 \underbrace{(1 - p_n^{-1}) \beta_n^i \beta_n^j}_{S_{ij}^{d,n}} + \lambda_0 \underbrace{\log J C_{ij}^{-1}}_{S_{ij}^v} \quad (\text{C.6a})$$

$$\bar{S}_{ij}^+ = \mu_0 \sum_n S_{ij}^{d,n} |_{p_n > 1} + \lambda_0 S_{ij}^v |_{J > 1}, \quad \bar{S}_{ij}^- = \mu_0 \sum_n S_{ij}^{d,n} |_{p_n < 1} + \lambda_0 S_{ij}^v |_{J < 1} \quad (\text{C.6b})$$

with β_n^i presents i -th element of n -th eigenvector β_n and the effective material tangent $\bar{\mathbb{D}}_{ijkl}$ and its negative/positive parts are given by

$$\bar{\mathbb{D}}_{ijkl} = 2\mu_0 \sum_{n=1}^3 [p_n^{-2} \beta_n^i \beta_n^j \beta_n^k \beta_n^l + (1 - p_n^{-1}) R_{n,ijkl}] + \lambda_0 \underbrace{(C_{ij}^{-1} C_{kl}^{-1} + 2\log J C_{ijkl})}_{\mathbb{D}_v} \quad (\text{C.7a})$$

$$\bar{\mathbb{D}}_{ijkl}^+ = 2\mu_0 \sum_n Q_{n,ijkl} |_{p_n > 1} + \lambda_0 \mathbb{D}_v |_{J > 1} \quad \bar{\mathbb{D}}_{ijkl}^- = 2\mu_0 \sum_n Q_{n,ijkl} |_{p_n < 1} + \lambda_0 \mathbb{D}_v |_{J < 1} \quad (\text{C.7b})$$

with

$$C_{ijkl} := -\frac{1}{2}(C_{ik}^{-1}C_{jl}^{-1} + C_{il}^{-1}C_{jk}^{-1}) \quad (\text{C.8a})$$

$$Q_{n,ijkl} := p_n^{-2}\beta_n^i\beta_n^j\beta_n^k\beta_n^l + (1 - p_n^{-1})R_{n,ijkl} \quad (\text{C.8b})$$

$$R_{n,ijkl} := \frac{\partial(\beta_n^i\beta_n^j)C_{kl}}{\partial} \quad (\text{C.8c})$$

An explicit expression of $R_{n,ijkl}$ is lengthy and one may follow Miehe and Lambrecht [63] to derive this.

For the volumetric/deviatoric decomposition of Amor et al. [7], the computation of ψ^\pm is greatly simplified as: If $J > 1$, $\psi^+ = \psi_0$, Else $\psi^+ = \psi_d$. The corresponding expressions of \bar{S}_{ij}^\pm and \bar{D}_{ijkl}^\pm can be obtained using same conditions on Eqs. (C.6) and (C.7). Calculations for Neo-Hookean-II are similar as Neo-Hookean-I and hence not repeated.

Appendix D. Finite element matrices

This appendix provides expressions for finite element matrices. For the sake of presentation, we confine to 2D problems, but extension to 3D is straightforward. The interpolation matrices $\mathbf{N} := [N_1, \dots, N_I, \dots]$ and $\bar{\mathbf{N}} := [\bar{N}_1, \dots, \bar{N}_I, \dots]$, and the gradient matrices $\mathbf{B} := [B_1, \dots, B_I, \dots]$ and $\bar{\mathbf{B}} := [\bar{B}_1, \dots, \bar{B}_I, \dots]$ have the following components,

$$\mathbf{N}_I(\mathbf{X}) = \begin{bmatrix} N_I & 0 \\ 0 & N_I \end{bmatrix}, \quad \mathbf{B}_I(\mathbf{X}) = \begin{bmatrix} \partial_X N_I & 0 \\ 0 & \partial_Y N_I \\ \partial_Y N_I & \partial_X N_I \end{bmatrix}, \quad \bar{\mathbf{N}}_I(\mathbf{X}) = N_I(\mathbf{X}), \quad \bar{\mathbf{B}}_I(\mathbf{X}) = \begin{bmatrix} \partial_X \bar{N}_I \\ \partial_Y \bar{N}_I \end{bmatrix} \quad (\text{D.1a})$$

where the notation $\partial_X f$ denotes the gradient of f with respect to X . As can be seen, the displacement field and damage field are interpolated using the same shape functions i.e., $\bar{N}_I(\mathbf{X}) = N_I(\mathbf{X})$. If required, different shape functions can be used, see e.g. Wu et al. [90].

The deformation gradient matrix is written as

$$\mathbf{F}(\mathbf{X}) = \begin{bmatrix} 1 + \sum \partial_X N_I u_{xI} & \sum \partial_Y N_I u_{xI} \\ \sum \partial_X N_I u_{yI} & 1 + \sum \partial_Y N_I u_{yI} \end{bmatrix} \quad (\text{D.1b})$$

where u_{xI} is the x -component of the displacement vector of node I . And \mathbf{B}_{0I} is given by

$$\mathbf{B}_{0I}(\mathbf{X}) = \begin{bmatrix} \partial_X N_I F_{11} & \partial_X N_I F_{21} \\ \partial_Y N_I F_{12} & \partial_X N_I F_{22} \\ \partial_X N_I F_{12} + \partial_Y N_I F_{11} & \partial_X N_I F_{22} + \partial_Y N_I F_{21} \end{bmatrix} \quad (\text{D.1c})$$

The expression for the geometrical part of the tangent matrix is lengthy. Thus, confining to three noded triangular elements, \mathbf{K}_{geo} is written as,

$$\mathbf{K}_{\text{geo}} = \begin{bmatrix} H_{11} & 0 & H_{12} & 0 & H_{13} & 0 \\ 0 & H_{11} & 0 & H_{12} & 0 & H_{13} \\ H_{21} & 0 & H_{22} & 0 & H_{23} & 0 \\ 0 & H_{21} & 0 & H_{22} & 0 & H_{23} \\ H_{31} & 0 & H_{32} & 0 & H_{33} & 0 \\ 0 & H_{31} & 0 & H_{32} & 0 & H_{33} \end{bmatrix} \quad H_{IJ} = \int_{\Omega_0} [\partial_X N_I \quad \partial_Y N_I] \begin{bmatrix} S_{xx} & S_{xy} \\ S_{xy} & S_{yy} \end{bmatrix} \begin{bmatrix} \partial_X N_J \\ \partial_Y N_J \end{bmatrix} dV \quad (\text{D.1d})$$

References

- [1] Alnaes M, Blechta J, Hake J, Johansson A, Kehlet B, Logg A, et al. The fenics project version 1.5. Arch Numer Softw 2015;3(100).
- [2] Alnaes MS, Logg A, Mardal KA, Skavhaug O, Langtangen HP. Unified framework for finite element assembly. Int J Comput Sci Eng 2009;4(4):231–44. <https://doi.org/10.1504/IJCSE.2009.029160>.
- [3] Alnaes MS, Logg A, Ølgaard KB, Rognes ME, Wells GN. Unified form language: A domain-specific language for weak formulations of partial differential equations. ACM Trans Math Softw 2014;40(2). <https://doi.org/10.1145/2566630>.
- [4] Ambati M, Gerasimov T, De Lorenzis L. A review on phase-field models of brittle fracture and a new fast hybrid formulation. Comput Mech 2015;55(2):383–405.
- [5] Ambati M, Kruse R, De Lorenzis L. A phase-field model for ductile fracture at finite strains and its experimental verification. Comput Mech 2016;57(1):149–67.
- [6] Amor H. Approche variationnelle des lois de Griffith et de Paris via des modeles non-locaux d'endommagement: Etude theorique et mise en oeuvre numerique [PhD thesis]. Paris, France: Université Paris 13; 2008.
- [7] Amor H, Marigo J-J, Maurini C. Regularized formulation of the variational brittle fracture with unilateral contact: Numerical experiments. J Mech Phys Solids 2009;57(8):1209–29.
- [8] Arruda EM, Boyce MC. A three-dimensional constitutive model for the large stretch behavior of rubber elastic materials. J Mech Phys Solids 1993;41(2):389–412.
- [9] Balay S, Buschelman K, Eijkhout V, Gropp W, Kaushik D, Knepley M, et al. PETSc Users Manual. ReVision 2010. <https://doi.org/10.2172/1178104>.
- [10] Belytschko T, Kam W, Moran B, Elkhodary KI. Nonlinear finite elements for continua and structures, 2nd ed. . Wiley; 2001. ISBN 9781118632703.
- [11] Benson SJ, Munson TS. Flexible complementarity solvers for large-scale applications. Optimiz Methods Softw 2006;21:155–68.
- [12] Borden M, Hughes T, Landis C, Verhoosel C. A higher-order phase-field model for brittle fracture: formulation and analysis within the isogeometric analysis framework. Comput Methods Appl Mech Eng 2014;273:100–18.

- [13] Borden MJ, Verhoosel CV, Scott MA, Hughes TJ, Landis CM. A phase-field description of dynamic brittle fracture. *Comput Methods Appl Mech Eng* 2012;217–220:77–95.
- [14] Borden MJ, Hughes TJ, Landis CM, Anvari A, Lee IJ. A phase-field formulation for fracture in ductile materials: Finite deformation balance law derivation, plastic degradation, and stress triaxiality effects. *Comput Methods Appl Mech Eng* 2016;312:130–66.
- [15] Bourdin B, Francfort G, Marigo J-J. Numerical experiments in revisited brittle fracture. *J Mech Phys Solids* 2000;48(4):797–826.
- [16] Bourdin B, Larsen CJ, Richardson CL. A time-discrete model for dynamic fracture based on crack regularization. *Int J Fract* 2011;168(2):133–43.
- [17] Braides A. Approximation of free-discontinuity problems. Berlin: Springer science & Business Media; 1998.
- [18] Chen C-H, Bouchbinder E, Karma A. Instability in dynamic fracture and the failure of the classical theory of cracks. *Nat Phys* 2017;13(12):1186.
- [19] Clayton JD, Knap J. A geometrically nonlinear phase field theory of brittle fracture. *Int J Fract* 2014;189(2):139–48.
- [20] De SK, White JR. Rubber technologist's handbook, vol. 1. iSmithers Rapra Publishing; 2001.
- [21] Elices M, Guinea G, Gomez J, Planas J. The cohesive zone model: advantages, limitations and challenges. *Eng Fract Mech* 2002;69(2):137–63.
- [22] Farrell P, Maurini C. Linear and nonlinear solvers for variational phase-field models of brittle fracture. *Int J Numer Meth Eng* 2017;109(5):648–67.
- [23] Feng D-C, Wu J-Y. Phase-field regularized cohesive zone model (czm) and size effect of concrete. *Eng Fract Mech* Jun 2018;197:66–79.
- [24] Francfort G, Marigo J-J. Revisiting brittle fracture as an energy minimization problem. *J Mech Phys Solids* 1998;46(8):1319–42.
- [25] Geuzaine C, Remacle JF. Gmsh: A 3-d finite element mesh generator with built-in pre- and post-processing facilities. *Int J Numer Meth Eng* 2009;79(11):1309–31.
- [26] Gim J, Schnitzer N, Otter LM, Cui Y, Motreuil S, Marin F, et al. Nanoscale deformation mechanics reveal resilience in nacre of *Pinna nobilis* shell. *Nat Commun* 2019;10(1):1–8.
- [27] Grady BP, Cooper SL. Thermoplastic elastomers. In: Science and technology of rubber. Elsevier; 2005. p. 555–617 [chapter 13].
- [28] Griffith AA. The phenomena of rupture and flow in solids. *Philos Trans R Soc Lond* 1920;221:163–98.
- [29] Gultekin O, Dal H, Holzapfel GA. A phase-field approach to model fracture of arterial walls: Theory and finite element analysis. *Comput Methods Appl Mech Eng* 2016;312:542–66.
- [30] Gultekin O, Dal H, Holzapfel GA. Numerical aspects of anisotropic failure in soft biological tissues favor energy-based criteria: A rate-dependent anisotropic crack phase-field model. *Comput Methods Appl Mech Eng* 2018;331:23–52.
- [31] Gupta A, Krishnan M, Chowdhury R, Chakrabarti A. An auto-adaptive sub-stepping algorithm for phase-field modeling of brittle fracture. *Theor Appl Fract Mech* 2020;102622.
- [32] Hale JS, Li L, Richardson CN, Wells GN. Containers for portable, productive, and performant scientific computing. *Comput Sci Eng* 2017;19(6):40–50.
- [33] Hesch C, Weinberg K. Thermodynamically consistent algorithms for a finite-deformation phase-field approach to fracture. *Int J Numer Meth Eng* 2014;99(12):906–24.
- [34] Hesch C, Gil A, Ortigosa R, Dittmann M, Bilgen C, Betsch P, et al. A framework for polyconvex large strain phase-field methods to fracture. *Comput Methods Appl Mech Eng* 2017;317:649–83.
- [35] Heydari-Meybodi M, Ayatollahi MR, Dehghany M, Berto F. Mixed-mode (I/II) failure assessment of rubber materials using the effective stretch criterion. *Theoret Appl Fract Mech* 2017;91:126–33.
- [36] Hirshkesh S, Natarajan S, Annabattula RK. A fenics implementation of the phase field method for quasi-static brittle fracture. *Front Struct Civ Eng* 2019a;13(2):380–96.
- [37] Hirshkesh S, Natarajan RK, Annabattula, Martínez-Páñeda E. Phase field modelling of crack propagation in functionally graded materials. *Compos Part B: Eng* 2019;169:239–48.
- [38] Hocine NA, Abdelaziz MN, Imad A. Fracture problems of rubbers: J-integral estimation based upon η factors and an investigation on the strain energy density distribution as a local criterion. *Int J Fract* 2002;117(1):1–23.
- [39] Holzapfel GA, Ogden RW. Constitutive modelling of arteries. *Proc R Soc A: Math Phys Eng Sci* 2010;466(2118):1551–97.
- [40] Holzapfel GA, Gasser TC, Ogden RW. A new constitutive framework for arterial wall mechanics and a comparative study of material models. *J Elast* 2000;61(1–3):1–48.
- [41] Irwin GR. Analysis of stresses and strains near the end of a crack traversing a plate. *J Appl Mech* 1957;24:361–4.
- [42] Kachanov L. Time rupture process under creep conditions. *Izv A Rad Nauk SSSR otd Tekh Nauk* 1958;8:26–31.
- [43] Kafaji IKA. Formulation of a dynamic material point method (MPM) for geomechanical problems [PhD thesis]. Germany: Universituy of Stuttgart; 2013.
- [44] Kirby RC, Logg A. A compiler for variational forms. *ACM Trans Math Softw* 2006;32(3). doi:10.1145/1163641.1163644.
- [45] Klinkel S, Govindjee S. Using finite strain 3D-material models in beam and shell elements. *Eng Comput* 2002;19(8):902–21.
- [46] Kristensen PK, Martínez-Páñeda E. Phase field fracture modelling using quasi-newton methods and a new adaptive step scheme. *Theor Appl Fract Mech* 2019;102446.
- [47] Kuhn C, Schuter A, Müller R. On degradation functions in phase field fracture models. *Comput Mater Sci* 2015;108(Part B):374–84.
- [48] Kumar A, Francfort GA, Lopez-Pamies O. Fracture and healing of elastomers: A phase-transition theory and numerical implementation. *J Mech Phys Solids* 2018;112:523–51.
- [49] Lee S, Wheeler MF, Wick T. Pressure and fluid-driven fracture propagation in porous media using an adaptive finite element phase field model. *Comput Methods Appl Mech Eng* 2016;305:111–32.
- [50] Li T. Gradient damage modeling of dynamic brittle fracture variational principles and numerical simulations [PhD thesis]. Paris: L'ecole Polytechnique de; 2016.
- [51] Loew PJ, Peters B, Beex L. Rate-dependent phase-field damage modeling of rubber and its experimental parameter identification. *J Mech Phys Solids* 2019;127:266–94.
- [52] Loew PJ, Peters B, Beex L. Fatigue phase-field damage modeling of rubber using viscous dissipation: Crack nucleation and propagation. *Mech Mater* 2020;142:103282.
- [53] Logg A, Wells GN. Dolfin: Automated finite element computing. *ACM Trans Math Softw* 2010;37(2). <https://doi.org/10.1145/1731022.1731030>.
- [54] Logg A, Mardal K-A, Wells GN, et al. Automated solution of differential equations by the finite element method. Springer; 2012. <https://doi.org/10.1007/978-3-642-23099-8>. ISBN 978-3-642-23098-1.
- [55] Lubomirsky Y, Chen CH, Karma A, Bouchbinder E. Universality and stability phase diagram of two-dimensional brittle fracture. *Phys Rev Lett* 2018;121(13):134301.
- [56] Malvern L. Introduction to the mechanics of a continuous medium. New Jersey: Prentice-Hall International; 1969.
- [57] Mandal TK, Nguyen VP, Heidarpour A. Phase field and gradient enhanced damage models for quasi-brittle failure: A numerical comparative study. *Eng Fract Mech* 2019;207:48–67.
- [58] Mandal TK, Nguyen VP, Wu J-Y. Length scale and mesh bias sensitivity of phase-field models for brittle and cohesive fracture. *Eng Fract Mech* 2019;217(106532).
- [59] Mandal TK, Nguyen VP, Wu J-Y. Evaluation of variational phase-field models for dynamic brittle fracture. *Eng Fract Mech* 2020;235. In press.
- [60] Mang K, Wick T, Wollner W. A phase-field model for fractures in nearly incompressible solids. *Comput Mech* 2019.
- [61] Martínez-Páñeda E, Golahmar A, Niordson CF. A phase field formulation for hydrogen assisted cracking. *Comput Methods Appl Mech Eng* 2018;342:742–61.
- [62] May S, Vignillet J, de Borst R. A numerical assessment of phase-field models for brittle and cohesive fracture: γ -convergence and stress oscillations. *Eur J Mech A Solids* 2015;52:72–84.
- [63] Miehe C, Lambrecht M. Algorithms for computation of stresses and elasticity moduli in terms of seth–hill's family of generalized strain tensors. *Commun Numer Methods Eng* 2001;17(5):337–53.
- [64] Miehe C, Schänzel LM. Phase field modeling of fracture in rubbery polymers. Part I: Finite elasticity coupled with brittle failure. *J Mech Phys Solids* 2014;65(1):93–113.
- [65] Miehe C, Hofacker M, Welschinger F. A phase field model for rate-independent crack propagation: Robust algorithmic implementation based on operator splits.

- Comput Methods Appl Mech Eng 2010;199(45–48):2765–78.
- [66] Miehe C, Welschinger F, Hofacker M. Thermodynamically consistent phase-field models of fracture: Variational principles and multi-field FE implementations. Int J Numer Meth Eng 2010;83(10):1273–311.
- [67] Miehe C, Schaezel L-M, Ulmer H. Phase field modeling of fracture in multi-physics problems. Part I. balance of crack surface and failure criteria for brittle crack propagation in thermo-elastic solids. Comput Methods Appl Mech Eng 2015;294:449–85.
- [68] Nguyen TT, Yvonnet J, Bornert M, Chateau C, Sab K, Romani R, Le Roy R. On the choice of parameters in the phase field method for simulating crack initiation with experimental validation. Int J Fract 2016;197(2):213–26.
- [69] Nguyen VP, Wu JY. Modeling dynamic fracture of solids with a phase-field regularized cohesive zone model. Comput Methods Appl Mech Eng 2018;340:1000–22.
- [70] Nguyen-Thanh C, Nguyen VP, de Vuorbeil A, Mandal TK, Wu JY. Jive: an open source, research-oriented C++ library for solving partial differential equations. Adv Eng Softw 2020;2(2):2.
- [71] Ølgaard KB, Wells GN. Optimisations for quadrature representations of finite element tensors through automated code generation. ACM Trans Math Softw 2010;37. <https://doi.org/10.1145/1644001.1644009>.
- [72] Park K, Paulino GH. Cohesive zone models: a critical review of traction-separation relationships across fracture surfaces. Appl Mech Rev 2011;64(6):060802.
- [73] Paul K, Zimmermann C, Mandadapu KK, Hughes TJR, Landis CM, Sauer RA. An adaptive space-time phase field formulation for dynamic fracture of brittle shells based on LR NURBS. arXiv:1906.10679 [cs]; June 2019.
- [74] Pham K, Amor H, Marigo J-J, Maurini C. Gradient damage models and their use to approximate brittle fracture. Int J Damage Mech 2011;20:618–52.
- [75] Pidaparti RM, Yang TY, Soedel W. Plane stress finite element prediction of mixed-mode rubber fracture and experimental verification. Int J Fract 1990;45(3):221–41.
- [76] Piero GD, Lancioni G, March R. A variational model for fracture mechanics: Numerical experiments. J Mech Phys Solids 2007;55(12):2513–37.
- [77] Rabczuk T. Computational methods for fracture in brittle and quasi-brittle solids: State-of-the-art review and future perspectives. ISRN Appl Math 2013. <https://doi.org/10.1155/2013/849231>.
- [78] Raina A, Miehe C. A phase-field model for fracture in biological tissues. Biomech Model Mechanobiol 2016;15(3):479–96.
- [79] Schlüter A, Willenbächer A, Kuhn C, Müller R. Phase field approximation of dynamic brittle fracture. Comput Mech 2014;54(5):1141–61.
- [80] Söderlind G, Wang L. Adaptive time-stepping and computational stability. J Comput Appl Math 2006;185(2): 225–43. ISSN 0377–0427. doi: 10.1016/j.cam.2005.03.008.
- [81] Talamini B, Mao Y, Anand L. Progressive damage and rupture in polymers. J Mech Phys Solids 2018;111:434–57.
- [82] Tang S, Zhang G, Guo TF, Guo X, Liu WK. Phase field modeling of fracture in nonlinearly elastic solids via energy decomposition. Comput Methods Appl Mech Eng 2019;347:477–94.
- [83] Tanné E, Li T, Bourdin B, Marigo JJ, Maurini C. Crack nucleation in variational phase-field models of brittle fracture. J Mech Phys Solids January 2018;110:80–99.
- [84] Tian F, Tang X, Xu T, Li L. An adaptive edge-based smoothed finite element method (ES-FEM) for phase-field modeling of fractures at large deformations; 2019.
- [85] Wu JY. A unified phase-field theory for the mechanics of damage and quasi-brittle failure in solids. J Mech Phys Solids 2017;103:72–99.
- [86] Wu JY, Nguyen VP. A length scale insensitive phase-field damage model for brittle fracture. J Mech Phys Solids 2018;119:20–42.
- [87] Wu J-Y, Huang Y, Nguyen VP. On the BFGS monolithic algorithm for the unified phase field damage theory. Comput Methods Appl Mech Eng 2019a;112704.
- [88] Wu J-Y, Nguyen VP, Nguyen CT, Sutula D, Sinaie S, Bordas SPA. Phase field modeling of fracture. Adv Appl Mech; 2019b:53.
- [89] Wu J-Y, Qiu J-F, Nguyen VP, Mandal TK, Zhuang L-J. Computational modeling of localized failure in solids: Xfem vs pf-czm. Comput Methods Appl Mech Eng 2019;345:618–43.
- [90] Wu J-Y, Mandal TK, Nguyen VP. A phase-field regularized cohesive zone model for hydrogen assisted cracking. Comput Methods Appl Mech Eng 2020;358:112614.
- [91] Wu JY, Nguyen VP, Zhou H, Huang Y. A variationally consistent phase-field anisotropic damage model for fracture. Comp Meth Appl Mech Eng 2020;358(112629).
- [92] Ye J-Y, Yin B-B, Zhang L-W, Reddy J. Large strained fracture of nearly incompressible hyperelastic materials: enhanced assumed strain methods and energy decomposition. J Mech Phys Solids 2020;103939.
- [93] Yin S, Yang W, Kwon J, Wat A, Meyers MA, Ritchie RO. Hyperelastic phase-field fracture mechanics modeling of the toughening induced by Bouligand structures in natural materials. J Mech Phys Solids 2019;131:204–20.
- [94] Zhang G, Guo TF, Guo X, Tang S, Fleming M, Liu WK. Fracture in tension-compression-asymmetry solids via phase field modeling. Comput Methods Appl Mech Eng 2019;357:112573.
- [95] Zienkiewicz OC, Taylor RL, F.D.D.. The finite element method for solid and structural mechanics. Elsevier; 2013.